

FULL-SKY GRAVITATIONAL LENSING SIMULATION FOR LARGE-AREA GALAXY SURVEYS AND COSMIC MICROWAVE BACKGROUND EXPERIMENTS

RYUICHI TAKAHASHI¹, TAKASHI HAMANA², MASATO SHIRASAKI², TOSHIYA NAMIKAWA^{3,4}, TAKAHIRO NISHIMICHI^{5,6},
KEN OSATO⁷, AND KOSEI SHIROYAMA¹

¹Faculty of Science and Technology, Hirosaki University, 3 Bunkyo-cho, Hirosaki, Aomori 036-8561, Japan

²National Astronomical Observatory of Japan, Mitaka, Tokyo 181-8588, Japan

³Department of Physics, Stanford University, Stanford, California 94305, USA

⁴Kavli Institute for Particle Astrophysics and Cosmology, SLAC National Accelerator Laboratory, Menlo Park, California 94025, USA

⁵Kavli Institute for the Physics and Mathematics of the Universe (WPI), The University of Tokyo Institutes for Advanced Study (UTIAS), The University of Tokyo, 5-1-5 Kashiwanoha, Kashiwa-shi, Chiba, 277-8583, Japan

⁶CREST, JST, 4-1-8 Honcho, Kawaguchi, Saitama, 332-0012, Japan

⁷Department of Physics, School of Science, The University of Tokyo, 7-3-1 Hongo, Bunkyo, Tokyo 113-0033, Japan

Draft version November 27, 2017

ABSTRACT

We present 108 full-sky gravitational lensing simulation data sets generated by performing multiple-lens plane ray-tracing through high-resolution cosmological N -body simulations. The data sets include full-sky convergence and shear maps from redshifts $z = 0.05$ to 5.3 at intervals of $150 h^{-1} \text{Mpc}$ comoving radial distance (corresponding to a redshift interval of $\Delta z \simeq 0.05$ at the nearby universe), enabling the construction of a mock shear catalog for an arbitrary source distribution up to $z = 5.3$. The dark matter halos are identified from the same N -body simulations with enough mass resolution to resolve the host halos of the Sloan Digital Sky Survey (SDSS) CMASS and luminous red galaxies (LRGs). Angular positions and redshifts of the halos are provided by a ray-tracing calculation, enabling the creation of a mock halo catalog to be used for galaxy-galaxy and cluster-galaxy lensing. The simulation also yields maps of gravitational lensing deflections for a source redshift at the last scattering surface, and we provide 108 realizations of lensed cosmic microwave background (CMB) maps in which the post-Born corrections caused by multiple light scattering are included. We present basic statistics of the simulation data, including the angular power spectra of cosmic shear, CMB temperature and polarization anisotropies, galaxy-galaxy lensing signals for halos, and their covariances. The angular power spectra of the cosmic shear and CMB anisotropies agree with theoretical predictions within 5% up to $\ell = 3000$ (or at an angular scale $\theta > 0.5$ arcmin). The simulation data sets are generated primarily for the ongoing Subaru Hyper Suprime-Cam survey, but are freely available for download at http://cosmo.phys.hirosaki-u.ac.jp/takahasi/allsky_raytracing/.

Subject headings: gravitational lensing: weak – large-scale structure of universe – cosmic background radiation

1. INTRODUCTION

Weak gravitational lensing is a powerful tool for probing the dark matter distribution and the nature of dark energy (see, e.g., a review by Hoekstra & Jain 2008; Munshi et al. 2008; Kilbinger 2015; Bartelmann & Maturi 2016). In this phenomenon, observed images of distant galaxies are coherently deformed by weak-lensing effects caused by foreground matter distribution. These distortions enable estimation of the density fluctuations in foreground matter through the correlation of background galaxy shapes (the so-called “cosmic shear”) and facilitate measurement of the mean mass profiles of foreground galaxies through stacking of the background shear fields (via so-called “galaxy-galaxy lensing”). The lensing signals are also sensitive to the amount of dark energy, in terms of both the distances to the sources (or lenses) and the growth rate of the density fluctuations.

The Canada-France-Hawaii Telescope Lensing Survey¹ (CFHTLenS) is a state-of-the-art weak-lensing survey that has observed 150 deg^2 and provided strong constraints on the amplitude of density fluctuations and

the matter density parameter (e.g., Heymans et al. 2012, 2013; Kilbinger et al. 2013). Several other larger-area surveys are also currently in progress. In the northern sky, the Subaru Hyper Suprime-Cam survey² (the HSC survey, hereafter) started their survey of 1400 deg^2 in 2014 (Miyazaki et al. 2012; Aihara et al. 2017), and in the southern sky, the Dark Energy Survey³ (DES) and the Kilo-Degree Survey⁴ (KiDS) are going to cover 5000 and 1500 deg^2 , respectively (de Jong et al. 2015; Dark Energy Survey Collaboration 2016a). DES and KiDS have already presented their first science results of cosmological parameter constraints obtained from cosmic shear data (Dark Energy Survey Collaboration 2016b; Hildebrandt et al. 2017). Beginning in 2020, the Large Synoptic Survey Telescope⁵ (LSST) plans to image half of the southern sky (e.g., Chang et al. 2013). In the 2020s, the space mission Euclid⁶ and the Wide Field In-

² <http://www.naoj.org/Projects/HSC/>

³ <https://www.darkenergysurvey.org/>

⁴ <http://kids.strw.leidenuniv.nl/>

⁵ <https://www.lsst.org/>

⁶ <http://sci.esa.int/euclid/>

¹ <http://www.cfhtlens.org>

frared Survey Telescope⁷ (WFIRST) plan to start large galaxy surveys.

The foreground matter also deforms the temperature and polarization patterns on the sky of the cosmic microwave background (CMB). The lensing of the CMB violates parity symmetry and produces a rotational pattern (B-mode) in CMB polarization (Zaldarriaga & Seljak 1998). The CMB lensing contains information on density fluctuations at relatively high redshift $z \simeq 1-3$ (e.g., Lewis & Challinor 2006). Precise measurements and removal of lensing-induced B-modes will be required to enhance sensitivity to B-modes that are generated by primordial gravitational waves (e.g., Kesden et al. 2002; Knox & Song 2002). The lensing signature was first detected by cross-correlating the Wilkinson Microwave Anisotropy Probe (WMAP) temperature map with a foreground galaxy distribution (Smith et al. 2007; Hirata et al. 2008). Lensing signals have also been detected using CMB data alone from multiple CMB experiments (POLARBEAR Collaboration 2014; SPTpol Collaboration 2014; BICEP2/Keck Array Collaborations 2016; Planck Collaboration 2016b; ACTPol Collaboration 2017). In ongoing and near-future CMB experiments such as those reported by the Simons Observatory⁸, SPT-3G⁹, and CMB-S4¹⁰, the nonlinear growth of the large-scale structure and post-Born corrections become important in the lensing analysis (Boehm et al. 2016; Pratten & Lewis 2016) and are detectable by measuring the bispectrum (Namikawa 2016) and higher-order cumulants (Liu et al. 2016). As these experiments will observe a wide area of CMB sky, a full-sky simulation including the effect of the nonlinear evolution will be required.

To extract cosmological information from the observational data, a large number of catalogs are necessary to estimate the covariances of observables (e.g., Takahashi et al. 2009). Mocks are useful in testing analysis tools that are to be used in forthcoming real observations. Because current weak-lensing surveys and CMB experiments cover large areas ($> 1000 \text{ deg}^2$), full-sky mocks covering the entire survey regions will be required. Furthermore, CMB and galaxy shear maps on the same sky region are not independent because they trace the same foreground matter distribution; therefore, mock catalogs for different probes that are consistently constructed out of the same foreground density fields are necessary for cross-correlation analyses. The observables and their covariances generally depend on the survey geometry and mask regions in a complicated manner (e.g., Takada & Hu 2013); as such, full-sky mocks will be useful for correctly incorporating this geometrical dependence into the analysis.

As weak lensing probes small scales ($\lesssim 10 \text{ Mpc}$), it is necessary to apply an N -body simulation-based ray-tracing technique to investigate the nonlinear gravitational evolution (e.g., Jain et al. 2000; Hamana & Mellier 2001; Vale & White 2003; Hilbert et al. 2009). Through such ray-tracing simula-

tions, non-Gaussian error can be naturally introduced from mode coupling between different scales into the cosmic-shear power spectrum (Cooray & Hu 2001). Furthermore, it is possible in such simulations to identify individual halos, which is necessary to locate the formation sites of galaxies for the study of galaxy-galaxy lensing. Previous authors have prepared a large number ($\gtrsim 100$) of mock catalogs to estimate the covariances of observables such as the convergence power spectrum (Sato et al. 2009; Kiessling et al. 2011; Harnois-Déraps et al. 2012; Harnois-Déraps & van Waerbeke 2015; Petri et al. 2016b), the correlation function (Sato et al. 2011; Harnois-Déraps et al. 2012; Harnois-Déraps & van Waerbeke 2015), galaxy-galaxy lensing (Shirasaki et al. 2015, 2017), and the three-point function (or bispectrum) of the convergence (Kayo et al. 2013; Sato & Nishimichi 2013). These mocks have also been used to estimate the probability distributions of the convergence or magnification (e.g., Hamana et al. 2000; Taruya et al. 2002; Das & Ostriker 2006; Hilbert et al. 2007; Takahashi et al. 2011) and the higher-order moments (skewness and kurtosis) of the convergence (e.g., Petri et al. 2016b; Shirasaki 2017).

Full-sky lensing simulations have previously been performed in CMB lensing studies (Carbone et al. 2008, 2009; Das & Bode 2008; Sehgal et al. 2010; van Engelen et al. 2014) and in studies of the statistical properties of the convergence field (Fosalba et al. 2008; Teyssier et al. 2009; Becker 2013; Fosalba et al. 2015a,b; Hamana et al. 2015; Shirasaki et al. 2015). The full-sky simulation we present here has several advantages over previous works: (1) because we generated a set of simulation data (weak-lensing maps, lensed CMB maps, and halo catalogs) from the same underlying density field, it is possible to study their cross-correlations in the form of galaxy-galaxy lensing, CMB lensing with cosmic shear, and CMB lensing with halo clustering; (2) because we do not employ the Born approximation, it is possible to study the post-Born effects in CMB lensing (note that very recently, Fabbian et al. (2017) also studied this topic); (3) we produced the largest sample of full-sky lensing simulation data to date, with 108 generated realizations.

Our simulation is designed primarily for the preparation of weak-lensing mock catalogs of the HSC survey. Because this survey covers $\sim 1400 \text{ sq. degrees}$, 20 mock HSC survey regions can be taken from a single full-sky map without overlap (Shirasaki et al. 2015), translating into ~ 2000 HSC mocks in total from the 108 full-sky maps. This large number enables us to calculate the covariances of observables with a reasonable accuracy ($\sim (2000/2)^{-1/2} \simeq 3\%$, see also Section 4). The simulation also resolves dark matter halos whose mass range comprehensively covers the SDSS CMASS galaxies of typical halo mass $\sim 10^{13} h^{-1} M_{\odot}$ at $0.4 < z < 0.8$ (e.g., White et al. 2011; Alam et al. 2015) and luminous red galaxies (LRGs) of halo mass $\sim 10^{13-14} h^{-1} M_{\odot}$ at $z < 0.5$ (e.g., Eisenstein et al. 2001; Zheng et al. 2009), making it possible to study galaxy-galaxy lensing and the cross correlation of the halo distribution with the CMB map.

In Section 2 we describe in detail our numerical sim-

⁷ <https://wfirst.gsfc.nasa.gov/>

⁸ <https://simonsobservatory.org/>

⁹ <https://pole.uchicago.edu/spt/>

¹⁰ <https://cmb-s4.org/>

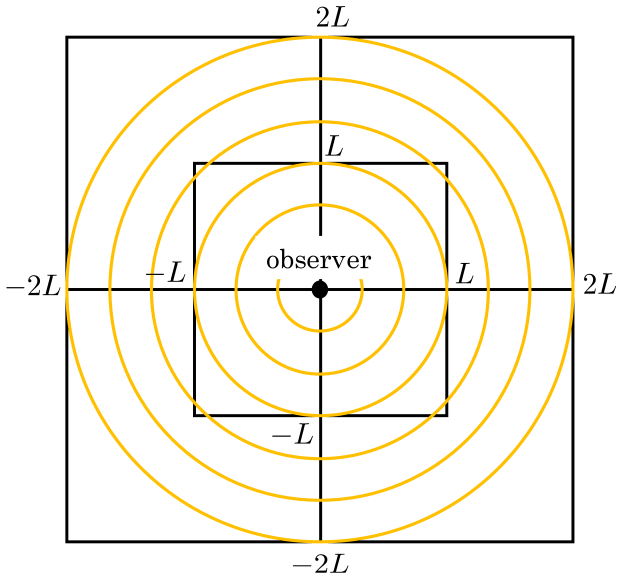


FIG. 1.— Configuration of ray-tracing simulation with cubic simulation boxes of lengths $L, 2L, 3L, \dots$, where $L = 450 h^{-1} \text{Mpc}$ (comoving scale), placed around the observer. The figure shows the inner two boxes with side lengths L and $2L$, respectively. The observer is located at the vertex of the boxes. In each box, we constructed three spherical shells with thickness of $\Delta r = L/3 = 150 h^{-1} \text{Mpc}$; the orange circles show the boundaries between the shells.

ulations and simulation products (which are further described in the appendices). We present the basic statistics of our data and compare them with theoretical models in Sections 3 and 4. In Section 5 we discuss known issues of our simulation data. A summary and discussion are presented in Section 6, and a guide to use the simulation products is provided in Appendix D and on the web¹¹. Throughout this paper, we adopt the standard ΛCDM (Lambda cold dark matter) cosmology that is consistent with the WMAP 9 years result (Hinshaw et al. 2013). The cosmological parameters are the CDM density parameter $\Omega_{\text{cdm}} = 0.233$, the baryon density $\Omega_{\text{b}} = 0.046$, the matter density $\Omega_{\text{m}} = \Omega_{\text{cdm}} + \Omega_{\text{b}} = 0.279$, the cosmological constant $\Omega_{\Lambda} = 0.721$, the Hubble parameter $h = 0.7$, the amplitude of density fluctuations $\sigma_8 = 0.82$, and the spectral index $n_s = 0.97$. We also adopt the natural units $c = G = 1$.

2. ALL-SKY RAY-TRACING SIMULATION

In this section, we describe our ray-tracing simulation. We prepared a system of nested cubic simulation boxes to reproduce the mass distribution in the Universe. The boxes had side lengths $L, 2L, 3L, \dots$, with $L = 450 h^{-1} \text{Mpc}$, and were placed around a fixed vertex representing the observer’s position, as shown in Figure 1. In this scheme, each box was duplicated eight times and placed around the observer using the periodic boundary conditions, and we constructed three spherical lens shells of width $\Delta r = 150 h^{-1} \text{Mpc}$ within each box period (see Figure 1). We then calculated the gravitational potential on the lens shells and traced the resulting light-ray paths from the observer to the last scattering surface. For basic equations and details of the multiple-plane gravi-

tational lensing algorithm and actual implementations for the numerical simulation, we refer the reader to Appendix C of Shirasaki et al. (2015).

2.1. *N*-body Simulations

We first conducted a cosmological *N*-body simulation on the periodic cubic box following the gravitational evolution of dark matter particles without baryonic processes. We generated the initial conditions based on the second-order Lagrangian perturbation theory (2LPT; Crocce et al. 2006; Nishimichi et al. 2009) with the initial linear power spectrum calculated using the Code for Anisotropies in the Microwave Background (CAMB; Lewis et al. 2000). We followed the gravitational evolution from the initial redshift using the *N*-body code GADGET2 (Springel et al. 2001; Springel 2005) with a softening length set to 4% of the mean particle separation. We prepared 14 boxes with side lengths $L = 450, 900, 1350, \dots, 6300 h^{-1} \text{Mpc}$ in steps of $450 h^{-1} \text{Mpc}$, with six independent copies at each box size, totaling 84 ($= 14 \times 6$) realizations in total. The number of particles for each box was 2048^3 , making the mass and spatial resolutions better for the inner boxes. The particle positions were dumped at redshifts corresponding to the comoving distances to the lens planes at $r = 150(i - 0.5) h^{-1} \text{Mpc}$ for $i = 1, 2, 3, \dots$. Table 1 summarizes our simulation settings, including box side lengths, particle masses, minimum halo masses (which were 50 times the particle masses), softening lengths, dumped redshifts, and initial redshifts.

We checked that the average matter power spectra of all six realizations agreed with theoretical predictions of the revised Halofit (Smith et al. 2003; Takahashi et al. 2012) within 5% (10%) for $k < 5(6) h \text{Mpc}^{-1}$ at $z < 1$, for $k < 0.8(1) h \text{Mpc}^{-1}$ at $z < 3$, and for $k < 0.5(0.7) h \text{Mpc}^{-1}$ at $z < 7$. Figure 19 in Appendix A shows a comparison of the measured power spectra with the Halofit prediction. The figure clearly shows the scales that are resolved.

2.2. Ray-tracing Simulation

We briefly explain the procedure we used to trace light rays through the *N*-body data. We used the public code GRAYTRIX,¹² which follows the standard multiple-lens plane algorithm in spherical coordinates (see Appendix C of Shirasaki et al. (2015) for a detailed description of the algorithm) using the HEALPix algorithm (Górski et al. 2005). As shown in Figure 1, we constructed three lens shells in each simulation box and projected the particle positions onto these shells. There were $12 \times N_{\text{side}}^2$ equal-area pixels on each shell in the HEALPix pixelization, and we computed the projected surface density by assigning each particle to the nearest pixel. The two-dimensional gravitational potential was solved via the Poisson equation using the multipole expansion. The deflection angle and Jacobian matrix were obtained from the first and second covariant derivatives of the potential (Becker 2013) using the HEALPix subroutines `map2alm` and `alm2map_der` to perform the computation. In our simulation, we adopted the three-pixel

¹¹ http://cosmo.phys.hirosaki-u.ac.jp/takahasi/allsky_raytracing/

¹² <http://th.nao.ac.jp/MEMBER/hamanatk/GRayTrix/>

TABLE 1
 N -BODY SIMULATION PARAMETERS

Box Size (h^{-1} Mpc)	Particle Mass ($h^{-1}M_{\odot}$)	Minimum Halo Mass ($h^{-1}M_{\odot}$)	Softening Length (h^{-1} kpc)	Dumped Redshift	Initial Redshift
450	8.2×10^8	4.1×10^{10}	8	0.025, 0.076, 0.129	63
900	6.6×10^9	3.3×10^{11}	16	0.182, 0.238, 0.294	63
1350	2.2×10^{10}	1.1×10^{12}	24	0.353, 0.413, 0.476	63
1800	5.3×10^{10}	2.6×10^{12}	32	0.541, 0.608, 0.678	49
2250	1.0×10^{11}	5.1×10^{12}	40	0.751, 0.827, 0.907	49
2700	1.8×10^{11}	8.9×10^{12}	48	0.990, 1.078, 1.170	49
3150	2.8×10^{11}	1.4×10^{13}	56	1.267, 1.370, 1.478	39
3600	4.2×10^{11}	2.1×10^{13}	64	1.593, 1.714, 1.844	39
4050	6.0×10^{11}	3.0×10^{13}	72	1.982, 2.130, 2.287	39
4500	8.2×10^{11}	4.1×10^{13}	80	2.456, 2.638, 2.833	31
4950	1.1×10^{12}	5.5×10^{13}	88	3.044, 3.272, 3.519	31
5400	1.4×10^{12}	7.1×10^{13}	92	3.788, 4.080, 4.400	31
5850	1.8×10^{12}	9.0×10^{13}	100	4.750, 5.135, 5.560	31
6300	2.3×10^{12}	1.1×10^{14}	108	6.030, 6.551, 7.133	31

NOTE. — The side length of the simulation box, the particle mass, the minimum halo mass, the softening length, the dumped redshift, and the initial redshift. The number of particles and realizations are 2048^3 and 6, respectively, for all the simulation boxes.

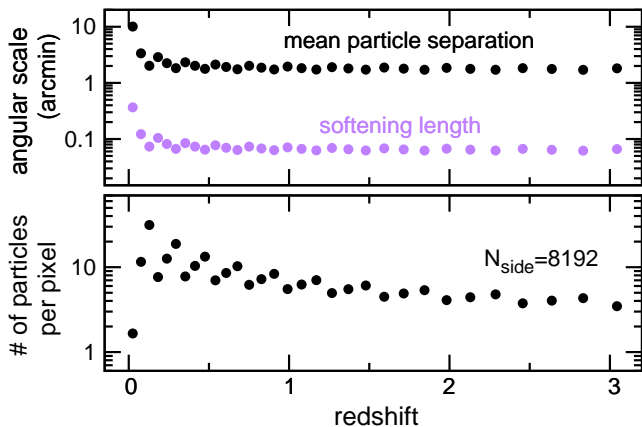


FIG. 2.— **Upper panel:** angular scales of mean particle separation (black dots) and softening length (purple dots) projected onto the lens plane. The x-axis is the redshift of the lens plane from $z = 0$ to 3. The softening length is 4% of the mean particle separation. **Lower panel:** particle number density per pixel on the lens shell at resolution $N_{\text{side}} = 8192$. The number density simply scales as $\propto N_{\text{side}}^{-2}$.

resolutions $N_{\text{side}} = 4096, 8192,$ and 16384 , corresponding to pixel sizes of 0.86, 0.43, and 0.21 arcmin, respectively. We chose 18 observer’s positions in each simulation box to increase the number of realizations¹³ (it is possible to choose an arbitrary observer’s position within the box under the periodic boundary condition), resulting in $18 \times 6 = 108$ realizations of lens shells at each redshift. We prepared 108 lens shells for $N_{\text{side}} = 4096$ and 8192 and a single shell for $N_{\text{side}} = 16384$. The simulation boxes were prepared up to redshift 7.1 (see Table 1); for higher redshifts up to the last scattering surface ($z = 7.1 - 1100$), we constructed lens shells assuming Gaussian surface density fluctuations based on the linear matter power spectrum.

The upper panel of Figure 2 plots the angular scales

¹³ The 18 positions are $(x, y, z) = (0, 0, 0), (L/2, 0, 0), (0, L/2, 0), (0, 0, L/2), (L/2, L/2, 0), (0, L/2, L/2), (L/2, 0, L/2), (L/2, L/2, L/2), (\pm L/4, 0, 0), (0, \pm L/4, 0), (0, 0, \pm L/4), (L/4, L/4, 0), (0, L/4, L/4), (L/4, 0, L/4),$ and $(L/4, L/4, L/4)$.

of mean particle separation (black dots) and softening length (purple dots) in the N -body data against the redshift of the lens plane (x -axis). As the angular scale of the mean particle separation (softening length) is typically ~ 2 (0.08) arcmin for $z \gtrsim 0.1$, the softening length is well below the angular pixel size. The lower panel plots the number of particles per pixel on the lens shell; the typical number density is about 2 – 10 for $N_{\text{side}} = 8192$ at $z \gtrsim 0.3$. Here the number density simply scales as $\propto N_{\text{side}}^{-2}$ for other pixel resolutions.

Finally, we traced the light-ray paths by solving lens equations to obtain the angular positions of light rays on the source planes. We also obtained full-sky maps of the convergence κ , shear $\gamma_{1,2}$, and rotation ω by solving the evolution equation of the Jacobian matrix along the light-ray path. Here, the Jacobian matrix is

$$A = \begin{pmatrix} 1 - \kappa - \gamma_1 & -\gamma_2 - \omega \\ -\gamma_2 + \omega & 1 - \kappa + \gamma_1 \end{pmatrix}. \quad (1)$$

The lens planes were placed at $r = 150(i - 0.5)h^{-1}\text{Mpc}$, while the source planes were at $r = 150i h^{-1}\text{Mpc}$, where $i = 1, 2, \dots$. These full-sky maps were prepared at every $150 h^{-1}\text{Mpc}$ comoving distance up to $z = 5.3$ and at the last scattering surface ($z = 1100$). Table 2 shows the output ID number of the source plane, the source redshift, and the comoving distance to the source. As mentioned above, we prepared 108 independent maps up to $z = 1100$ for $N_{\text{side}} = 4096$ and 8192 and a single map up to $z = 5.3$ for $N_{\text{side}} = 16384$. The high-resolution map with $N_{\text{side}} = 16384$ will be used to check the numerical convergence at small scale (near the pixel size).

Note that we randomly chose the lens planes to perform the ray-tracing simulation but avoided using the same plane more than once. As we used three lens planes taken from each given box as a single set, the matter distribution along the line-of-sight direction is continuous at the boundaries between the lens planes within each box, but discontinuous between planes taken from different-sized boxes. As a result, the radial structure appears continuous within the effective shell thickness of $450 h^{-1}\text{Mpc}$ (not $150 h^{-1}\text{Mpc}$). Note that the thickness of the lens shell slightly affects the convergence and

TABLE 2
N-BODY SIMULATION PARAMETERS

output ID number	source redshift	distance (h^{-1} Mpc)
zs1	0.051	150
zs2	0.102	300
zs3	0.155	450
zs4	0.210	600
zs5	0.266	750
zs6	0.323	900
zs7	0.383	1050
zs8	0.444	1200
zs9	0.508	1350
zs10	0.574	1500
zs11	0.643	1650
zs12	0.714	1800
zs13	0.788	1950
zs14	0.866	2100
zs15	0.948	2250
zs16	1.033	2400
zs17	1.123	2550
zs18	1.218	2700
zs19	1.318	2850
zs20	1.423	3000
zs21	1.535	3150
zs22	1.653	3300
zs23	1.778	3450
zs24	1.912	3600
zs25	2.055	3750
zs26	2.207	3900
zs27	2.370	4050
zs28	2.546	4200
zs29	2.734	4350
zs30	2.937	4500
zs31	3.156	4650
zs32	3.393	4800
zs33	3.651	4950
zs34	3.931	5100
zs35	4.237	5250
zs36	4.571	5400
zs37	4.938	5550
zs38	5.342	5700
zs66	1100	9900

NOTE. — The output ID number of the source plane, the source redshift, and the comoving distance to the source. There are 108 full-sky maps each for $N_{\text{side}} = 4096$ and 8192, and there is a single map for $N_{\text{side}} = 16384$ from zs1 to zs38.

shear power spectra (as we discuss in Section 3 and in Appendix B).

2.3. Halo Catalogs

We constructed halo catalogs using the public code ROCKSTAR (Behroozi et al. 2013), which identifies halos based on the six-dimensional phase-space friends-of-friends algorithm. The masses of the identified structures were then determined according to the spherical overdensity around the center. The minimum halo mass, given in Table 1, was set to 50 times the particle mass. The catalogs effectively cover the SDSS CMASS and LOWZ galaxy ranges, in which the halo masses are $M \gtrsim 10^{13} M_{\odot}$. Smaller halos can be resolved at lower redshifts. The following halo data provided by ROCKSTAR’s default outputs were stored: the virial mass M_{vir} ; the spherical overdensity masses within several radii, M_{200b} (the radius at a mean halo density 200 times larger than the background density) and $M_{200c, 500c, 2500c}$ (the radii at 200, 500, and 2500 times larger than the cosmo-

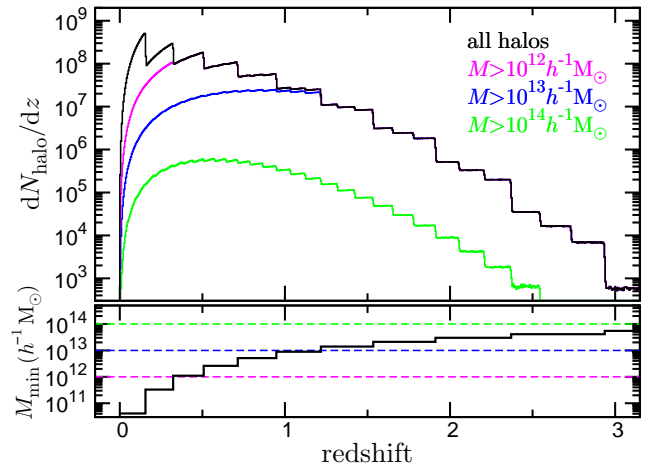


FIG. 3.— **Upper panel:** halo number distribution as a function of redshift. The vertical axis shows the halo number at redshift interval z to $z + dz$ in the overall sky. The black line is the result for all the halos, while the red, blue, and green lines are for heavier halos $M_{200b} > 10^{12} h^{-1} M_{\odot}$, $10^{13} h^{-1} M_{\odot}$, and $10^{14} h^{-1} M_{\odot}$, respectively. **Lower panel:** minimum halo mass ($M_{200b, \text{min}}$) as a function of redshift. The horizontal dashed lines denote $M_{200b} = 10^{12} h^{-1} M_{\odot}$ (magenta), $10^{13} h^{-1} M_{\odot}$ (blue), and $10^{14} h^{-1} M_{\odot}$ (green), respectively.

logical critical density, respectively); the halo central position and velocity; the virial radius and scale radius obtained by fitting the Navarro-Frenk-White (NFW) profile (Navarro et al. 1997); and the halo ID. The catalogs also contain subhalos and their parent halo IDs (we used the ROCKSTAR utility `find_parents` to identify these subhalos).

The ROCKSTAR halo catalogs of each cubic box were combined in layers of lens shells to form full-sky light-cone halo catalogs. To convert the (three-dimensional) halo positions and velocities into projected angular positions and radial velocities on the sky, we used the light-ray paths obtained from the ray-tracing simulation (see Appendix C3 of Shirasaki et al. (2015) for technical details of the conversion). The redshifts of halos were derived from the radial distances and peculiar velocities. The angular halo positions are given both on the image plane (i.e., the first lens plane) and the lens plane onto which the halo is projected. As we used 18 spherical shells from each simulation box, a given halo appears several times on the various maps; however, as the halos are projected onto different directions, they have different orientations.

We checked that the halo mass function in our simulation agrees with the Tinker mass function (Tinker et al. 2008) within 12% for $z < 1.2$ and 30% for $z < 2.0$. We also checked that the linear halo bias measured in our simulation is consistent with the fitting formula (Tinker et al. 2010) within 10% at $k < 0.4 h \text{Mpc}^{-1}$ and $z < 0.5$ for $M_{200b} = 10^{12} h^{-1} M_{\odot}$, at $k < 0.4 h \text{Mpc}^{-1}$ and $z < 1.4$ for $M_{200b} = 10^{13} h^{-1} M_{\odot}$, and at $k < 0.3 (0.1) h \text{Mpc}^{-1}$ and $z < 0.9 (1.5)$ for $M_{200b} = 10^{14} h^{-1} M_{\odot}$, respectively. Figures 20 and 21 in Appendix A plot comparisons of the simulation results with the theoretical fitting formulae for the halo mass function and the halo bias, respectively. These figures clearly show the halo-mass and redshift ranges that are validated.

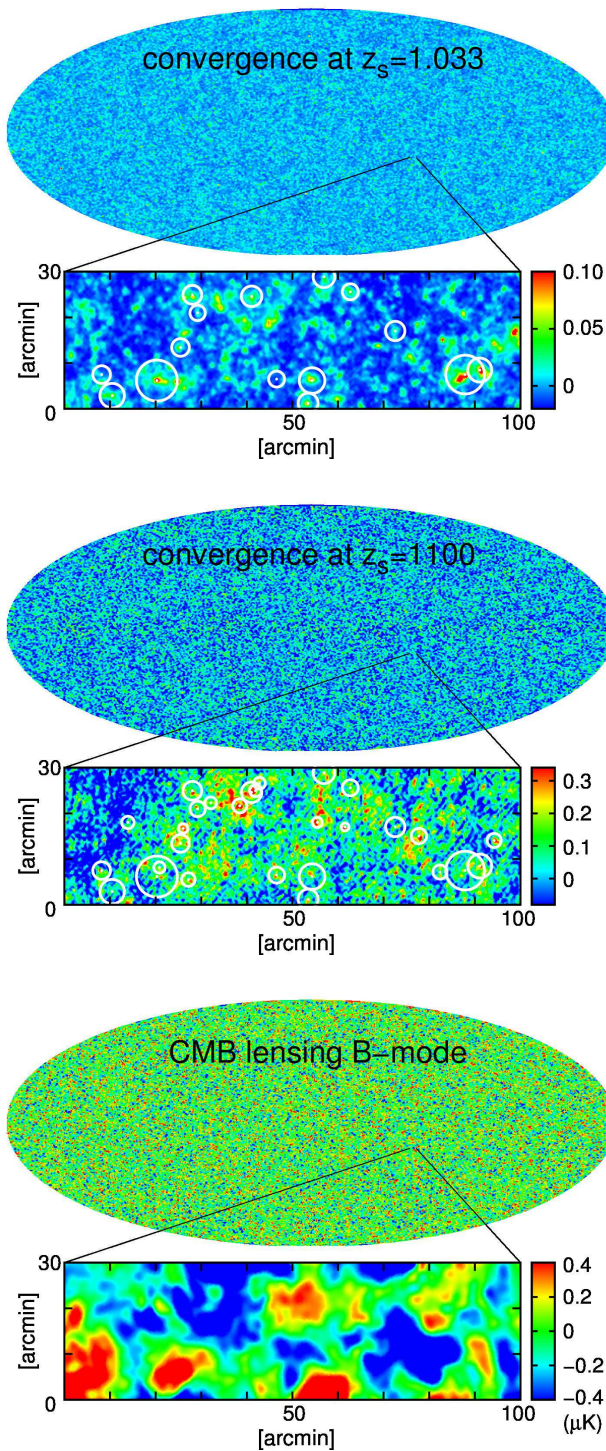


FIG. 4.— **Top panel:** contour plot of the convergence at source redshift $z_s = 1.033$. The lower rectangular panel is a zoom-in map of size $100 \times 30 \text{ arcmin}^2$. The white dots with circles indicate positions of foreground massive halos of $M_{200b} > 6 \times 10^{13} h^{-1} M_\odot$, where the circle radius corresponds to the virial radius on the sky. **Middle panel:** same as the top panel, but at the last scattering surface ($z_s = 1100$). **Bottom panel:** same as the above panels, but for the CMB lensing B-mode. The three full-sky maps in the figure are taken from the same realization, and the three rectangular panels also show the same region.

The upper panel of Figure 3 plots the halo number density on the full sky as a function of redshift, with the y-axis showing the number of halos in the redshift interval z to $z+dz$. The figure shows the average number density of the 108 maps. The black line represents all halos heavier than the minimum halo mass, while the magenta, blue, and green lines indicate halos heavier than 10^{12} , 10^{13} , and $10^{14} h^{-1} M_\odot$, respectively. Thus, our simulation can resolve halos of mass 10^{12} , 10^{13} , and $10^{14} h^{-1} M_\odot$ up to $z = 0.3$, 1.2 , and 3.5 , respectively (see also the lower panel, which plots the minimum halo mass as a function of redshift). The total halo number is $\sim 1.3 \times 10^8$ up to $z = 6$ in a single map. The halo number density is discontinuous at several redshifts because (i) the dumped redshifts of the N -body simulation are discrete, and (ii) the minimum halo mass suddenly changes owing to changes in the mass resolution (see Table 1).

The top and middle panels of Figure 4 show contour plots of the convergence at $z_s = 1.033$ and 1100 , respectively. Each panel shows a full-sky map with a zoom-in map ($100 \times 30 \text{ arcmin}^2$). The resolution of the map shown here is $N_{\text{side}} = 8192$. In the zoom-in maps, the white dots with circles indicate the foreground halo positions, with the radius of each white circle corresponding to the virial radius of the corresponding halo on the sky. As clearly seen in the figure, the massive halos correspond to the high convergence peaks (we will calculate the mean convergence profiles of the halos in Section 3.3). However, some halos do not correspond to any high peak because they are very close to the observer or to the source and therefore the lensing efficiency is low. Small-scale noisy fluctuations on the zoom-in map can be seen at $z_s = 1100$ as a result of shot noise caused by the finite number density of dark matter particles in the N -body simulation. As the number density of particles decreases for higher redshifts (see Table 1), the shot noise appears more significant for higher source redshifts.

2.4. Lensed CMB Maps

In this subsection, we present the procedure we used to construct the lensed CMB temperature and polarization maps. The procedure is as follows: (1) we prepared the unlensed CMB temperature and polarization spectra using CAMB, ignoring any primordial B-modes; (2) based on the input angular power spectrum, we constructed 108 unlensed maps with Gaussian fluctuations using the `synfast` routine in `HEALPix` with $N_{\text{side}} = 8192$; and (3) finally, we evaluated the angular position shifts on the last scattering surface using the ray-tracing simulations with $N_{\text{side}} = 4096$ and 8192 . Under the transformations in step (3), the temperature and polarization fields were moved from angular position θ to $\theta + \mathbf{d}$, where \mathbf{d} is the deflection angle. To do this, we required accurate interpolation on the pixels (because the lensed ray positions were generally not at the centers of pixels) and also had to take the rotation of the polarization basis into account, which was dependent on the position on the sphere (this rotation was significant around the north and south poles). To do this, we employed the `LensPix` scheme (Challinor & Lewis 2005) to transform the maps¹⁴. Furthermore, we used the multiple-lens scattering (instead

¹⁴ We used the subroutine `HealpixInterpLensedMap_GradPhi` in `LensPix` with the parameters $\ell_{\text{max}} = 3N_{\text{side}}$ and `interp_factor` =

of the Born approximation), which generated a non-zero rotation of polarization (the so-called post-Born corrections: Cooray & Hu 2002; Hirata & Seljak 2003). In summary, we transferred the complex polarization field $(Q+iU)(\boldsymbol{\theta})$ to the new field $(\tilde{Q}+i\tilde{U})(\boldsymbol{\theta})$ using the deflection angle \mathbf{d} and the rotation of polarization β as (e.g., Marozzi et al. 2016; Lewis et al. 2017)

$$(\tilde{Q} + i\tilde{U})(\boldsymbol{\theta}) = e^{-2i\beta(\boldsymbol{\theta})}(Q + iU)(\boldsymbol{\theta} + \mathbf{d}), \quad (2)$$

where Q and U are the Stokes parameters. We constructed 108 lensed CMB maps for each resolution $N_{\text{side}} = 4096$ and 8192 .

Analytic expressions of polarization rotation β were derived by Marozzi et al. (2016) and Lewis et al. (2017) based on the perturbative expansion of gravitational potential but with different approximation schemes. Marozzi et al. (2016) used a post-Born approximation with a leading correction from multiple-lensing deflections and found that β is the same as the field rotation ω given in Equation (1), resulting in β of order 10^{-3} rad. Lewis et al. (2017), on the other hand, used the Born approximation, but took into account corrections from multiple-lensing deflections and the emission-angle effect, and found that the rotation angle is quadratic in the deflection angle and is very small ($\beta \approx 10^{-6}$ rad). In what follows, we consider two cases: one is $\beta = 0$ as a default, and the other is $\beta = \omega$.¹⁵ This difference will affect only the CMB B-mode power spectrum by a few percent for the very small scale $\ell > 2000$ (Section 3.5).

The bottom panel of Figure 4 shows a contour plot of the amplitude of the CMB lensing B-mode. The polarization patterns can be decomposed into E-mode (positive parity) and B-mode (negative parity). The HEALPix scheme (`map2alm`) automatically evaluates the multipole coefficients $a_{\ell m}$ of the polarization for the E- and B-modes separately from the full-sky map. We can then transform the B-mode coefficient to the contour map using the multipole expansion. A typical B-mode patterns size in the panel, as determined by the peak of the B-mode power spectrum, is a few 10 arcmin (we calculate the angular power spectra of the temperature and polarization fluctuations in Section 3.4).

3. BASIC STATISTICS

In this section, we present detailed comparisons between our simulation results and theoretical predictions for the convergence power spectrum (Section 3.1), shear correlation functions (Section 3.2), halo-galaxy lensing (Section 3.3), angular correlation function of halos (Section 3.4), and finally CMB power spectra (Section 3.5). We will show the measurements with two resolutions, $N_{\text{side}} = 4096$ and 8192 , to clearly show the angular scales that are resolved in each N_{side} .

3.1. Convergence Power Spectrum

1.5. We slightly modified the code to read the deflection-angle data obtained in our simulation.

¹⁵ We set $\beta = \omega$ in the previous version of our draft (arXiv:1706.01472v1). The field rotation ω at the last scattering surface can be numerically obtained from the ray-tracing simulation.

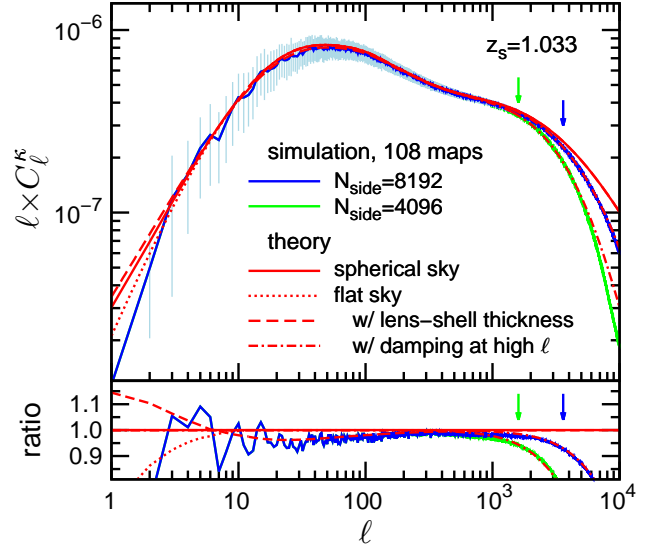


FIG. 5.— Convergence power spectrum $\ell \times C_\ell^\kappa$ as a function of the multipole ℓ at source redshift $z_s = 1.033$. The blue and green curves show the average power spectra of the 108 maps for angular resolutions $N_{\text{side}} = 8192$ and 4096 , respectively. The light-blue bars show the standard deviations of the 108 maps. The solid (dotted) red curve is the theoretical prediction of the spherical-sky (flat-sky) formula. The dashed curve takes into account the effects of the finite thickness of the lens shells (see Appendix B for a detailed discussion). The dot-dashed curves include a damping factor at high ℓ arising from the finite angular resolution. The down arrows indicate the scale at which the simulation results converge within 5%. The bottom panel shows ratios to the solid red curve.

Images of distant sources are distorted by the foreground mass distribution. This distortion is usually characterized by convergence and shear components. The convergence field at a source redshift z_s is, at the lowest order, given by the weighted surface mass density as (e.g., Bartelmann & Schneider 2001)

$$\kappa(\boldsymbol{\theta}) = \frac{3H_0^2\Omega_m}{2} \int_0^{z_s} \frac{dz}{H(z)} \frac{r(z)(r_s - r(z))}{a(z)r_s} \delta(r\boldsymbol{\theta}, r; z), \quad (3)$$

where $H(z)$ is the Hubble expansion rate at z , $a(z) = 1/(1+z)$ is the scale factor, $r(z)$ is the comoving distance to the redshift z , $r_s (= r(z_s))$ is the distance to the source, and $\delta(\boldsymbol{x}; z)$ is the density contrast at position \boldsymbol{x} at z . Here, we decompose the position \boldsymbol{x} into the radial distance r and the perpendicular distance $r\boldsymbol{\theta}$ in Equation (3). The convergence power spectrum in the flat-sky approximation is given by

$$C_\ell^\kappa = \frac{9H_0^4\Omega_m^2}{4} \int_0^{z_s} \frac{dz}{H(z)} \frac{(r_s - r(z))^2}{a(z)^2 r_s^2} P_\delta\left(k = \frac{\ell}{r(z)}; z\right), \quad (4)$$

where ℓ is the multipole and $P_\delta(k; z)$ is the power spectrum of the density contrast at wavenumber k at redshift z . In this expression, we use the revised Halofit formula for the nonlinear matter power spectrum (Smith et al. 2003; Takahashi et al. 2012).

Figure 5 shows the average convergence power spectrum at $z_s = 1.033$ evaluated from the 108 maps. The blue and green curves correspond to the resolutions at $N_{\text{side}} = 8192$ and 4096 , respectively (in this plot, we do not bin the results). We used the `map2alm` and `alm2c1` HEALPix schemes to measure the power spectra from the

maps. The dotted red curve shows the theoretical prediction in the flat-sky approximation given in Equation (4). We also consider a correction of the sky curvature at large angular scales, with the solid red curve including the correction proposed in Hu (2000) assuming a linear power spectrum of gravitational potential. The theoretical prediction of cosmic shear power spectra on the sphere includes the density power spectrum between different cosmological epochs for a given wavenumber, indicating that some approximations are required to evaluate such unequal-time cross spectra (e.g., see Kitching et al. 2017; Kilbinger et al. 2017, for details¹⁶). As the spherical-sky formula in Hu (2000) is valid only in the linear regime, we simply connect the spherical-sky formula to the flat-sky formula at an intersection point¹⁷ in plotting the solid curve. Although the spherical-sky formula gives 38%, 16%, and 9% higher amplitudes than the flat-sky formula for $\ell = 1, 2$, and 3, respectively, the difference is smaller than 5% (1%) for $\ell \geq 4$ (8). The differences between the two formulae are smaller than the standard deviations of the 108 samples at low multipoles (shown as the light-blue bars). The bottom panel shows the ratio of the simulation results to the theoretical prediction of the spherical-sky formula. For very small scales ($\ell > 10^3$), the simulation results underestimate the power owing to a lack of angular resolution. The dot-dashed curves take the finite angular resolution into account based on a simple damping factor at small scales

$$C_\ell^\kappa \rightarrow \frac{C_\ell^\kappa}{1 + (\ell/\ell_{\text{res}})^2}. \quad (5)$$

By setting a damping scale $\ell_{\text{res}} = 1.6 \times N_{\text{side}}$, the dot-dashed curve closely fits the simulation results. At intermediate scales ($\ell \simeq 10 - 100$), the simulation results are slightly lower than those of the theoretical model shown in the bottom panel (but the difference is less than 5%). This is because the finite thickness of the lens shells influences the angular power spectrum of surface density fluctuations on a shell (a detailed discussion of this is given in Appendix B). To take this effect into account, we convolved the matter power spectrum with the window function of the shell. The dashed curve shows the results of replacing the power spectrum $P_\delta(k, z)$ in Equation (4) by the convolved spectrum $P_\delta^W(k, z)$ in Equation (B8). This replaced curve agrees closely with the simulation results. In summary, our simulation results agree with theoretical prediction within 5% at $\ell < 3000$ (1400) for $N_{\text{side}} = 8192$ (4096).

We further checked that the convergence power spectrum at $N_{\text{side}} = 8192$ (4096) agrees with the higher-resolution result at $N_{\text{side}} = 16384$ within 5% for $\ell < 3600$ (1600) at $z_s = 0.3 - 5$. The down blue and green arrows in Figure 5 indicate the scales at which the simulation results converge.

3.2. Shear Correlation Functions

We next discuss the correspondence between our results and theoretical values for the shear correlation func-

¹⁶ Kilbinger et al. (2017) showed that the flat-sky power spectrum (4) was valid within 5% (1%) for $\ell > 5$ (20) for the CFHTLenS source redshift distribution (see their Figure 1).

¹⁷ The spherical-sky (flat-sky) formula predicts larger power at larger (smaller) scales. They intersect at $\ell = 13$ in our setting.

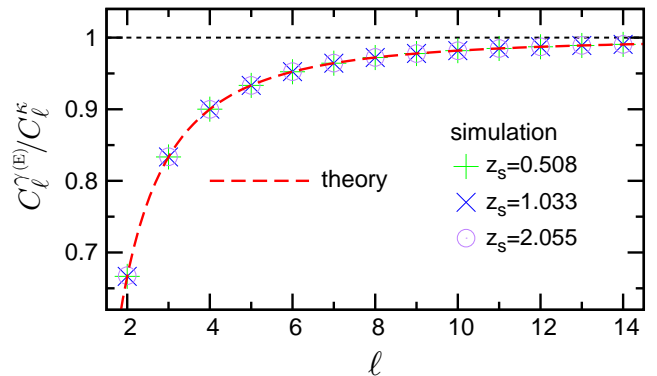


FIG. 6.— Ratio of $C_\ell^{\gamma^{(E)}}$ to C_ℓ^κ for $z_s = 0.508$ (green pluses), 1.033 (blue crosses), and 2.055 (purple circles). Here, $C_\ell^{\gamma^{(E)}}$ and C_ℓ^κ are the averages measured from the 108 maps with $N_{\text{side}} = 8192$. The dashed red curve denotes the theoretical prediction in the spherical sky, given in Equation (8).

tions. The shear components $\gamma_{1,2}$ are defined in the HEALPix spherical coordinates in the standard manner, where γ_1 is a component along a line of longitude (from the north pole to the south pole) and γ_2 is a component rotated by 45° (see also Figure 5 of the HEALPix primer¹⁸ for the coordinate convention). The shear can be decomposed into tangential and cross modes in terms of the relative angular position between two points. The tangential mode γ_t is defined along a great arc connecting two points, while the cross mode γ_\times is a mode rotated by 45° . The correlation of the shears at two angular positions θ_i and θ_j is then given by (e.g., Kaiser 1992; Schneider et al. 2002)

$$\xi_\pm^\gamma(\theta) = \langle [\gamma_t(\theta_i)\gamma_t(\theta_j) \pm \gamma_\times(\theta_i)\gamma_\times(\theta_j)] \rangle, \quad (6)$$

where θ is the angular separation between θ_i and θ_j (see also Kilbinger et al. 2013, Section 3.2, for a discussion about angular correlation functions in spherical coordinates). Note that the $\xi_\pm^\gamma(\theta)$ are independent of the coordinate system and $\xi_\pm^\gamma(\theta)$ is the same as the convergence correlation function in the flat-sky approximation.

The relation between the shear correlation functions and the angular power spectra in spherical coordinates is discussed in detail in previous works (e.g., Stebbins 1996; Hu & White 1997; Kamionkowski et al. 1997; Zaldarriaga & Seljak 1997; Ng & Liu 1999; Hu 2000). The shear power spectrum is generally decomposed into E- and B-modes. According to the previous works, the shear correlation functions $\xi_\pm^\gamma(\theta)$ can be rewritten in terms of the multipole expansion of the E/B-mode shear power spectra $C_\ell^{\gamma^{(E/B)}}$ as

$$\xi_\pm^\gamma(\theta) = \sum_{\ell=2}^{\infty} \sqrt{\frac{2\ell+1}{4\pi}} [C_\ell^{\gamma^{(E)}} \pm C_\ell^{\gamma^{(B)}}] {}_2Y_{\ell\mp 2}(\theta, 0), \quad (7)$$

where ${}_2Y_{\ell m}(\theta, \phi)$ are the spin-2 spherical harmonics. The shear E-mode and convergence power spectra are related

¹⁸ <http://healpix.sourceforge.net/documentation.php>

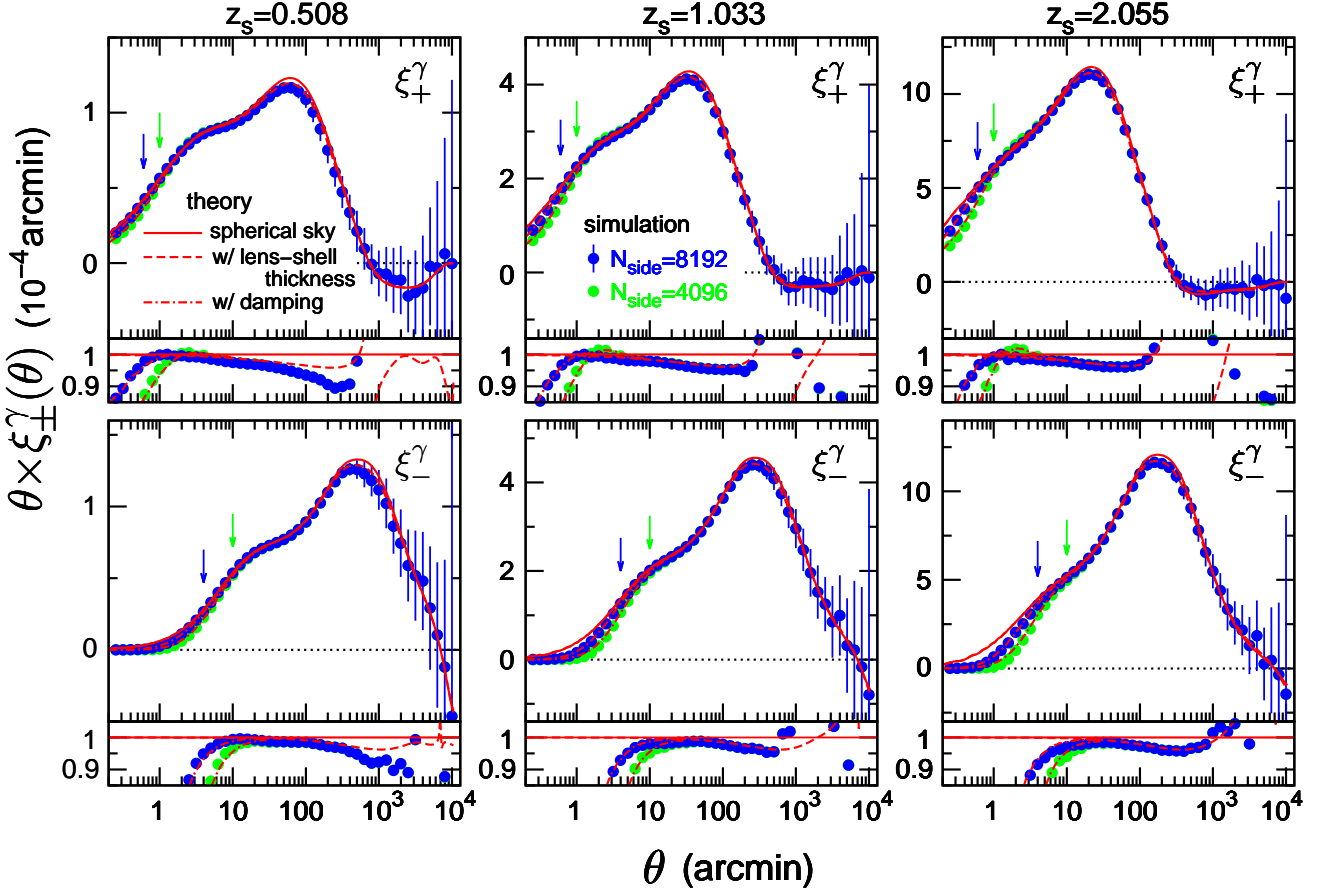


FIG. 7.— Shear correlation functions $\xi_{\pm}^{\gamma}(\theta)$ as a function of θ at source redshifts $z_s = 0.508, 1.033,$ and 2.055 (left to right panels, respectively). The upper (lower) panels plot ξ_{+}^{γ} (ξ_{-}^{γ}). The y -axes give $\theta \times \xi_{\pm}^{\gamma}(\theta)$ in units of 10^{-4} arcmin. The blue and green filled circles are the averages of the 108 maps with $N_{\text{side}} = 8192$ and 4096 , respectively. The blue error bars show the standard deviations. The solid red curves show the theoretical prediction in the spherical-sky formula. The dashed and dot-dashed curves include corrections for lens-shell thickness and finite angular resolution, respectively. The down blue and green arrows indicate the scales at which the simulation results converge within 5%. The small bottom panels show ratios to the solid red curves.

via (e.g., Becker 2013)

$$C_{\ell}^{\gamma(\text{E})} = \frac{(\ell+2)(\ell-1)}{\ell(\ell+1)} C_{\ell}^{\kappa}. \quad (8)$$

Figure 6 plots the ratio $C_{\ell}^{\gamma(\text{E})}/C_{\ell}^{\kappa}$ measured from the full-sky maps (denoted by the colored symbols) compared to the theoretical prediction of $[(\ell+2)(\ell-1)]/[\ell(\ell+1)]$ (the dashed red curve), showing that this relation (8) holds in our simulation. Note that in the small-angle limit, ${}_2Y_{\ell m}(\theta, \phi)$ is approximated by ${}_2Y_{\ell \mp 2}(\theta, 0) \simeq \sqrt{\ell/(2\pi)} J_{0/4}(\ell\theta)$, where $J_{0/4}(x)$ is the zeroth-order or fourth-order Bessel function. In this case, Equation (7) reduces to the flat-sky formula

$$\xi_{\pm}^{\gamma}(\theta) \simeq \frac{1}{2\pi} \int_0^{\infty} d\ell \ell \left[C_{\ell}^{\gamma(\text{E})} \pm C_{\ell}^{\gamma(\text{B})} \right] J_{0/4}(\ell\theta). \quad (9)$$

Figure 7 shows, from left to right, the shear correlation functions at $z_s = 0.508, 1.033,$ and 2.055 . The top (bottom) panels show ξ_{+}^{γ} (ξ_{-}^{γ}). The filled circles with error bars are the averages with standard deviations of the 108 maps. The data points are binned with $\Delta \log[\theta(\text{arcmin})] = 0.1$. To measure the correlation functions from the maps, we employed the multipole expansion of the power spectra in Equation (7). We evalu-

ated the shear E- and B-mode power spectra ($C_{\ell}^{\gamma(\text{E})}$ and $C_{\ell}^{\gamma(\text{B})}$) from the maps using the HEALPix scheme and then computed the summation (7) up to $\ell_{\text{max}} = 3N_{\text{side}}$. Here we do not include the shape noise for the analysis of the shear maps. The solid red curves show the theoretical prediction given in Equations (7) and (8). Here, we adopt the spherical-sky formula for C_{ℓ}^{κ} (see Section 3.1), but simply assume $C_{\ell}^{\gamma(\text{B})} = 0$ because the B-mode $C_{\ell}^{\gamma(\text{B})}$ is approximately three orders of magnitude smaller than the E-mode $C_{\ell}^{\gamma(\text{E})}$ at $\ell < 10^4$ (Cooray & Hu 2002; Krause & Hirata 2010). The dashed and dot-dashed curves include the effects of lens-shell thickness and finite angular resolution, respectively. These curves are the same as in Figure 5, but simply transformed into the correlation functions using the multipole expansion (7). The small bottom panels show ratios to the spherical-sky theoretical model. As seen in the small bottom panels, the simulation results are slightly smaller ($\lesssim 5\%$) than the theoretical model at intermediate scales ($\theta \sim 10 - 1000$ arcmin), although the difference can be attributed to the shell-thickness effect (the dashed curves). The simulation results at $z_s = 0.508$ show slightly more suppression than the theoretical prediction (the dashed curves) at interme-

TABLE 3
HALO SAMPLES

Name	Mass ($h^{-1}M_{\odot}$)	Redshift	Number of Halos
sample 1	$M_{200b} > 10^{13}$	$0.47 < z < 0.59$	2.2×10^6
sample 2	$M_{200b} > 10^{13.5}$	$0.16 < z < 0.36$	3.6×10^5
sample 3	$M_{200b} > 10^{14}$	$0.10 < z < 0.33$	5.8×10^4

NOTE. — The halo sample name, the minimum halo mass, the redshift range, and the number of halos in the all-sky sample. Sample 1,2, and 3 roughly correspond to the CMASS galaxy-like, LRG-like, and redMaPPer cluster-like samples.

diate scales ($\theta \sim 100 - 1000$ arcmin) because the theoretical model including the shell-thickness effect is less accurate in nearby lens planes at $z < 0.1$ (see also Appendix B). The scatter in the simulation results at large scales ($\theta > \text{several } 100$ arcmin) is caused by sample variance. The suppressions of ξ_{\pm}^{γ} at small scales ($\theta \lesssim 1 - 10$ arcmin) arise from the lack of angular resolution, which can be fitted well by including the damping factor (5) (the dot-dashed curves). In particular, the suppressions are significant for ξ_{-}^{γ} compared to ξ_{+}^{γ} , because ξ_{-}^{γ} is more sensitive to higher multipoles of the power spectrum (the spherical harmonics ${}_2Y_{\ell 2}(\theta, 0)$ have a first peak at higher ℓ than ${}_2Y_{\ell - 2}(\theta, 0)$ for a given θ) in Equation (7), and therefore ξ_{-}^{γ} is more influenced by this suppression at large ℓ . In summary, the simulation results for ξ_{+}^{γ} and ξ_{-}^{γ} at $N_{\text{side}} = 8192$ (4096) agree with the theoretical prediction within 5% at $\theta > 0.6$ (1) arcmin and $\theta > 6$ (10) arcmin, respectively.

We also confirmed that the shear correlation functions ξ_{+}^{γ} and ξ_{-}^{γ} at $N_{\text{side}} = 8192$ (4096) agree with those at the higher resolution $N_{\text{side}} = 16384$ within 5% for $\theta > 0.6$ (1.0) arcmin and for $\theta > 4$ (10) arcmin, respectively, within the redshift range $z_s = 0.3 - 5$. The down blue and green arrows in Figure 7 indicate the respective scales at which the convergence occurs.

3.3. Halo-galaxy Lensing

In this subsection, we calculate the mean convergence and tangential shear profiles of halos. The cross correlation of foreground galaxies with background shear can provide the excess surface mass density of foreground galaxies (galaxy-galaxy lensing). Combining galaxy-galaxy lensing with the galaxy clustering enables the inference of galaxy bias, which helps to break the degeneracy between cosmological parameters (e.g., Seljak et al. 2005). In addition, it is also possible to measure the mean density profile of clusters in this manner.

The Planck Collaboration (2016b) recently provided a convergence map reconstructed from temperature and polarization data. The SPT collaboration also published a full-sky convergence map reconstructed from SPT-SZ and Planck temperature maps (Omori et al. 2017). Several authors subsequently measured the mean mass profile of galaxies by correlating the foreground galaxies with the background convergence field (e.g., Miyatake et al. 2016b; Singh et al. 2017). The Planck convergence map has also been used to study the cross-correlation measurement with galaxy density (e.g., Giannantonio et al. 2016).

Here, we calculate for demonstration purposes the mean convergence and tangential shear profiles of three halo samples in Table 3 for two sources of background

galaxies at $z_s = 1.033$ and the CMB at $z_s = 1100$. The table summarizes the minimum halo mass, redshift range, and number of the halos for each sample. Samples 1,2, and 3 roughly correspond to the SDSS CMASS galaxy-like sample (Alam et al. 2015; Miyatake et al. 2015), the LRG-like sample (Reid et al. 2010; Mandelbaum et al. 2013), and the redMaPPer cluster-like sample (Rykoff et al. 2014; Miyatake et al. 2016a), respectively. We did not include subhalos in this analysis and also ignored the shape noise of the background field. Using the halo catalogs (see Section 2.3), we directly calculated the mean profiles of the foreground halos. The mean convergence profile at a separation R from the halo center can be written as

$$\langle \kappa \rangle (R) = \frac{1}{N_h} \sum_{i=1}^{N_h} \frac{1}{N_{\text{pix}(i)}} \sum_{j=1}^{N_{\text{pix}(i)}} \kappa(R_{ij}), \quad (10)$$

where R is the projected comoving separation, N_h is the number of halos in the sample, R_{ij} is the separation of the i th halo from the j th background convergence field, and $N_{\text{pix}(i)}$ is the number of pixels in the convergence map around the i th halo in an annulus with radius $R - \Delta R/2 < R_{ij} < R + \Delta R/2$. The mean tangential shear profile $\langle \gamma_t \rangle (R)$ is the same, but with κ simply replaced by γ_t in the above equation. We calculated the profiles using a brute-force direct summation of all pairs in the 108 maps.

To check our simulation results, we adopted two theoretical models of the halo model (e.g., Cooray & Sheth 2002) and the dark emulator (T. Nishimichi et al. in preparation). We briefly explain the halo model considered here for comparison. Essentially, we followed the halo model parameters employed in Oguri & Hamana (2011) (see also Oguri & Takada 2011), which can reproduce the simulation results of the mean convergence profile very well (Sato et al. 2009). The mean convergence at a (comoving) separation of R can be formally written as

$$\langle \kappa \rangle (R) = \frac{1}{N_h} \int_{z_1}^{z_2} dz \frac{dV}{dz} \int_{M_{\text{min}}}^{\infty} dM \frac{dn}{dM}(M, z) \kappa(R; M, z), \quad (11)$$

with the number of halos

$$N_h = \int_{z_1}^{z_2} dz \frac{dV}{dz} \int_{M_{\text{min}}}^{\infty} dM \frac{dn}{dM}(M, z),$$

where dV/dz ($= 4\pi r(z)^2/H(z)$) is the comoving volume element, z_1 and z_2 are the redshift range of the halos, M_{min} is the minimum halo mass given in Table 3, and dn/dM is the halo mass function for which we employ the fitting formula in Tinker et al. (2008). Here, we use the mass contained within the spherical overdensity region with a density 200 times higher than the mean (comoving) background density $\bar{\rho}_m$, i.e., $M_{200b} = 200\bar{\rho}_m \times (4\pi r_{200b}^3)/3$, where r_{200b} is the (comoving) halo radius. The convergence $\kappa(R; M, z)$ in Equation (11) comprises two terms: the halo density profile (the so-called ‘‘one-halo term’’), and the matter distribution around the halo (the so-called ‘‘two-halo term’’). For the density profile, we adopted an NFW profile with a truncation at large radius (Navarro et al. 1997;

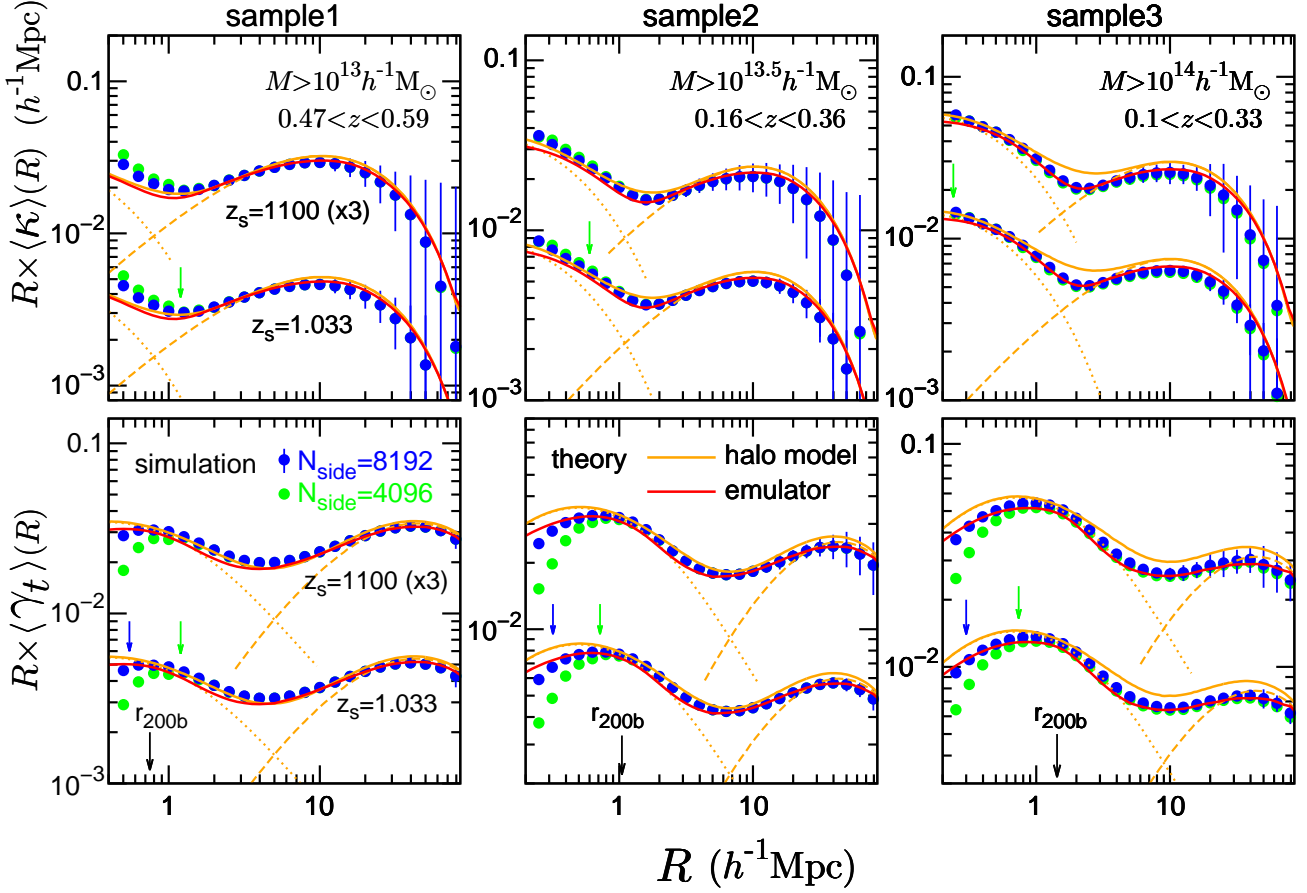


FIG. 8.— Mean convergence (upper panels) and tangential shear (lower panels) profiles of halos for the three halo samples described in Table 3. The x -axes are the (comoving) projected separations R from the halo centers, while the y -axes are the mean profiles. The source redshifts are $z_s = 1.033$ and 1100 , where the results with $z_s = 1100$ are multiplied by a factor three for clearer presentation. The blue and green symbols are the average simulation results of the 108 maps with a bin width of $\Delta \log[R/(h^{-1}\text{Mpc})] = 0.1$ at $N_{\text{side}} = 8192$ and 4096 , respectively, with the blue bars showing the standard deviations. The dotted (dashed) orange curves are the one-halo (two-halo) terms in the halo model, while the solid orange curves show their sums. The solid red curves indicate the theoretical prediction of the dark emulator (T. Nishimichi et al. 2017, in preparation). The down black arrows in the lower panels indicate the mean halo radius, r_{200b} , for each sample. The down blue and green arrows indicate the scales at which the simulation results converge to within 5% accuracy.

Baltz et al. 2009)

$$\rho(r) = \frac{\rho_s}{(r/r_s)(1+r/r_s)^2 [1+(r/r_t)^2]^2}, \quad (12)$$

where the truncation radius was set to $r_t = 3r_{200b}$. To determine the characteristic scale r_s , we employed a fitting formula of the concentration parameter $c = r_{200b}/r_s$ calibrated by an N -body simulation (Duffy et al. 2008). The characteristic density ρ_s is determined by using Equation (12) to determine the mass inside r_{200b} as $M_{200b} = 4\pi \int_0^{r_{200b}} dr r^2 \rho(r)$. Note that ρ_s and r_s depend on both M and z . Based on the halo surface mass density of $\Sigma(R) = \int_{-\infty}^{\infty} dl \rho[(R^2 + l^2)^{1/2}]$, the one-halo term is given by the surface density divided by the critical density, $\kappa_{1h}(R; M, z) = \Sigma(R; M, z)/\Sigma_{\text{crit}}(z)$ with $\Sigma_{\text{crit}}(z) = (1+z)r_s/[4\pi r(z)(r_s - r(z))]$.

The two-halo term represents the cross correlation between the halo and the surrounding matter,

$$\kappa_{2h}(R; M, z) = \frac{b_h(M, z)\bar{\rho}_m}{\Sigma_{\text{crit}}(z)} \int \frac{kdk}{2\pi} J_0(kR) P_{\text{m,lin}}(k; z), \quad (13)$$

where $P_{\text{m,lin}}$ is the linear matter power spectrum (cal-

culated by CAMB) and $J_0(x)$ is the zeroth-order Bessel function. We used the fitting formula of the halo bias $b_h(M, z)$ in Tinker et al. (2010). The convergence was calculated as the sum of the one- and two-halo terms: $\kappa(R; M, z) = \kappa_{1h}(R; M, z) + \kappa_{2h}(R; M, z)$. Inserting these terms into Equation (11) produced the mean convergence profile of the halos.

The tangential shear profile is similar to the convergence profile, but simply given by (e.g., Schneider et al. 2006, Section 2.3 of Part 3)

$$\langle \gamma_t \rangle(R) = \langle \bar{\kappa} \rangle(< R) - \langle \kappa \rangle(R), \quad (14)$$

where $\langle \bar{\kappa} \rangle(< R)$ is the mean convergence profile inside R , $\langle \bar{\kappa} \rangle(< R) = (2/R^2) \int_0^R dR' R' \langle \kappa \rangle(R')$.

We also employed the dark emulator constructed on a series of N -body simulations, which will soon be publicly available (T. Nishimichi et al., in preparation). Cosmological N -body simulations with 2048^3 particles were performed for 100 six-parameter w CDM cosmological models sampled around the Planck 2015 best-fit flat Λ CDM cosmology (Planck Collaboration 2016a) with 21 outputs dumped over a redshift range of $z = 0 - 1.5$. An efficient sampling scheme based on the maxi-min

distance Latin Hypercube design and the use of functional interpolation based on Gaussian processes allowed for an accurate prediction of the statistical quantities with a relatively small number of sampled points (see e.g., Heitmann et al. 2009, 2010; Lawrence et al. 2010 for earlier studies on the nonlinear matter power spectrum and Heitmann et al. 2016 for recent developments by the Mira-Titan Universe project). The `dark emulator` focuses on the halo clustering properties and provides the halo mass function, and auto- and cross-correlation functions of the halo and matter fields. The correlation functions are measured using a hybrid direct-FFT algorithm to achieve both accuracy (on scales smaller than the FFT grid) and speed. The excess surface mass density of halos can be obtained from the halo-mass cross-correlation function by convolving the appropriate kernel with a quick implementation of the Fourier transform (FFTLg, Hamilton 2000). T. Nishimichi et al. (in preparation) developed a python package in which the hyper-parameters for the Gaussian processes and the data table are prepared to enable a quick evaluation of the related statistical quantities for a given redshift, halo mass, and cosmological parameters. The current version presented here is based on 40 simulations with a box size of $1 h^{-1}\text{Gpc}$ at 40 different cosmological parameters. The statistics are derived for central halos identified by ROCKSTAR.

Figure 8 shows, from left to right, the mean convergence (upper panels) and tangential shear profile (lower panels) for halo samples 1 to 3. The source redshifts are $z_s = 1.033$ and 1100 . The filled blue and green circles are the averaged results of the 108 maps at $N_{\text{side}} = 8192$ and 4096 , respectively. The error bars show the standard deviations of the 108 maps. We excluded the subhalos from the samples. The solid orange and red curves show the theoretical predictions produced by the halo model and the `dark emulator`, respectively. The dotted and dashed orange curves show the one- and two-halo terms in the halo model. The `dark emulator` provides closer agreement, particularly at the intermediate scale between the one- and two-halo regimes. For smaller scales of $R \lesssim 1 h^{-1}\text{Mpc}$, the simulation results deviate from the theoretical models owing to the finite angular resolution. This corresponds to angular scales of $\sim 3 \text{ arcmin} [R/(h^{-1}\text{Mpc})][r/(h^{-1}\text{Gpc})]^{-1}$ (where r is the distance to the halo), which are comparable to the angular resolution of the shear correlation functions shown in Figure 7. The convergence profiles show a damping feature at larger scales ($R \gtrsim 30 h^{-1}\text{Mpc}$) compared to the theoretical predictions. This is partially a result of the lens-shell thickness effect underestimating the correlation. The separation $R \approx 30 h^{-1}\text{Mpc}$ corresponds to an angular scale $\theta \approx 100 \text{ arcmin}$, at which the suppression seen in Figure 7 is significant. In summary, the simulation results at $N_{\text{side}} = 8192$ agree with both theoretical models within 30% for the convergence profiles at $0.5 \leq R/(h^{-1}\text{Mpc}) \leq 40$ and for the tangential shear profiles at $0.4 \leq R/(h^{-1}\text{Mpc}) \leq 100$.

The down blue and green arrows in Figure 7 indicate the innermost scales at which the mean profiles for $\langle \kappa \rangle$ and $\langle \gamma_t \rangle$ at $N_{\text{side}} = 8192$ (4096) agree with the corresponding higher resolution $N_{\text{side}} = 16384$ profiles within 5%.

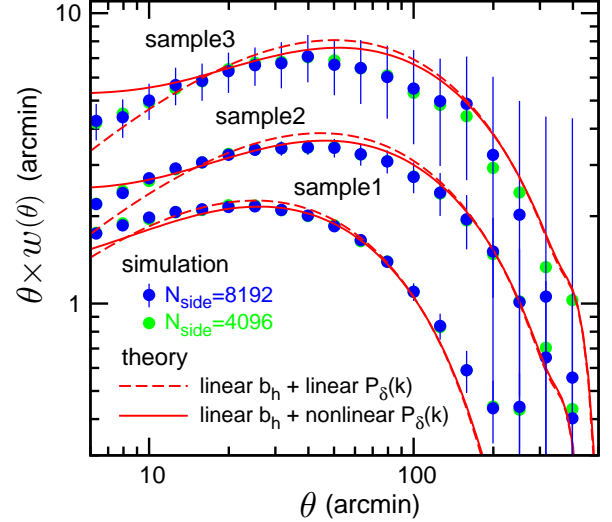


FIG. 9.— Halo angular correlation functions for samples from 1 to 3 (in Table 3), shown bottom to top, respectively. The blue and green circles with error bars are the averages with standard deviations of the 108 maps at $N_{\text{side}} = 8192$ and 4096 , respectively. The solid (dashed) red curves show the theoretical prediction in Equation (16) assuming linear halo bias and a nonlinear (linear) matter power spectrum.

3.4. Halo Clustering

In this subsection, we calculate the angular two-point correlation function of the halo samples in Table 3. The number density contrast of halos $\delta_h(\mathbf{x}; M, z)$ and the matter density contrast $\delta(\mathbf{x}; z)$ are related via $\delta_h(\mathbf{x}; M, z) = b_h(M, z)\delta(\mathbf{x}; z)$. Then, the projected halo number density contrast is given by

$$\delta_h^{2D}(\boldsymbol{\theta}) = \frac{1}{N_h} \int_{z_1}^{z_2} dz \frac{dV}{dz} \int_{M_{\min}}^{\infty} dM \frac{dn}{dM}(M, z) \times b_h(M, z) \delta(r\boldsymbol{\theta}, r; z), \quad (15)$$

where the term dn/dM is necessary to take into account the halo mass distribution in each sample (e.g., Cooray & Sheth 2002). The angular two-point halo correlation can be obtained from the above equation under the Limber approximation as (e.g., Dodelson 2003)

$$\begin{aligned} w(\boldsymbol{\theta}) &= \langle \delta_h^{2D}(\boldsymbol{\theta} + \boldsymbol{\theta}') \delta_h^{2D}(\boldsymbol{\theta}') \rangle \\ &= \frac{8\pi}{N_h^2} \int_{z_1}^{z_2} \frac{dz}{H(z)} \left[r(z) \int_{M_{\min}}^{\infty} dM \frac{dn}{dM}(M, z) b_h(M, z) \right]^2 \\ &\quad \times \int d\ell \ell P_\delta \left(k = \frac{\ell}{r(z)}; z \right) J_0(\ell\theta). \end{aligned} \quad (16)$$

where $P_\delta(k; z)$ is the matter power spectrum. We then calculated the halo correlation function $w(\theta)$ for the three halo samples in Table 3.

Figure 9 plots the angular correlation functions of halos from the three samples. The blue and green dots with error bars are the averages with standard deviations of the 108 maps at $N_{\text{side}} = 8192$ and 4096 , respectively. In this case, we first calculated the halo angular power spectra from the maps, subtracted the shot noise, and finally transformed the results into angular correlation functions using the multipole expansion. The solid (dashed) red curves show the theoretical prediction (Equation 16) with the nonlinear (linear) matter power

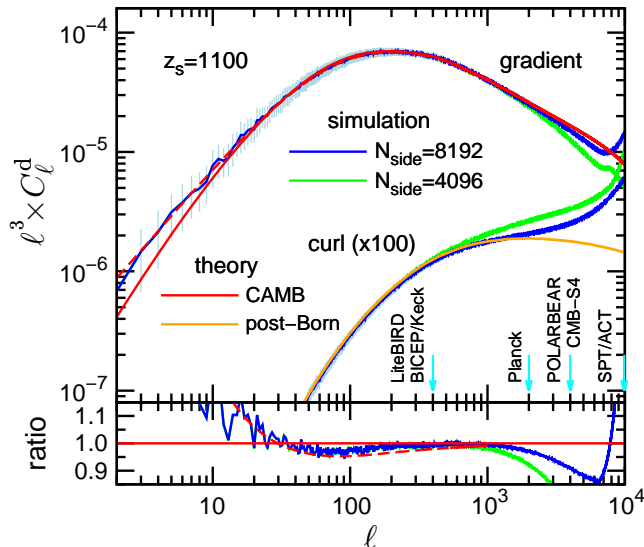


FIG. 10.— Deflection-angle power spectrum $\ell^3 \times C_\ell^d$ at the last scattering surface ($z_s = 1100$). Here, we plot the gradient and curl modes separately (with the curl mode C_ℓ^d multiplied by 100). The blue and green curves show the average simulation results from the 108 maps at $N_{\text{side}} = 8192$ and 4096, respectively. The light-blue bars give the standard deviations. The solid red (orange) curve is the theoretical prediction calculated by CAMB (using the post-Born corrections in Krause & Hirata (2010)). The dashed red curve is the same as the solid red curve (CAMB), but includes the lens-shell thickness effect. The down cyan arrows indicate the typical angular resolutions of CMB experiments. The bottom panel shows the ratios of the gradient mode results to those in CAMB.

spectrum. We employed the revised Halofit to derive the nonlinear matter power spectrum and the Tinker fitting functions to derive the mass function and linear halo bias, as was done in Section 3.3. The error bars for sample 3 are somewhat larger than the others because the shot noise is dominant even at relatively large scales of $\ell \gtrsim 70$ (corresponding to an angular scale of $\theta \lesssim 150$ arcmin).

Note that the radial distribution of halos is discontinuous at every $450 h^{-1} \text{Mpc}$ distance, which is caused by the boundaries between the different box sizes (see Table 1). As a result of this effect, we could not calculate the three-dimensional halo clustering across the boundaries. However, note also that these discontinuities do not affect any two-dimensional observables (e.g., cosmic shear, galaxy-galaxy lensing, or CMB lensing). These will affect only three-dimensional observables like a halo power spectrum (or correlation function).

3.5. Power Spectra of CMB Anisotropies

In this subsection, we calculate the angular power spectra of the CMB deflection angle and lensed CMB temperature and polarization. The deflection angle can be decomposed into two parts using the parity symmetry, $\mathbf{d} = \nabla\phi + (\star\nabla)\Omega$, where \star is the 90° rotation operator¹⁹, and the first and second terms are the gradient and curl modes, respectively (Hirata & Seljak 2003). The scalar and pseudo-scalar lensing potential, ϕ and Ω , are obtained by solving the Poisson equations $\nabla^2\phi = \nabla \cdot \mathbf{d}$ and $\nabla^2\Omega = (\star\nabla) \cdot \mathbf{d}$, respectively. Although the gravitational lensing by density fluctuations in linear theory does not

¹⁹ The a th component of the derivative is $(\star\nabla)^a = \epsilon^{ab}\nabla_b$ where ϵ^{ab} is the two-dimensional Levi-Civita symbol.

generate the curl mode under the Born approximation, the multiple-lens scattering employed in our simulation leads to a non-zero curl mode (Pratten & Lewis 2016). This curl mode is also generated by any vector or tensor metric perturbation (Namikawa et al. 2012; Saga et al. 2015).

Figure 10 shows the power spectrum of the deflection angle for both modes: the upper (lower) curves correspond to the gradient (curl) mode. We used the HEALPix subroutine (`alm2map_spin`) to calculate the power spectrum for each mode separately. The blue (green) curves with light-blue bars show averages with standard deviations for the 108 maps with $N_{\text{side}} = 8192$ (4096). The solid red curve shows the theoretical prediction by CAMB, in which we employed the revised Halofit for the nonlinear matter power spectrum. The orange curve shows the leading correction to the Born approximation (the so-called “post-Born correction”) predicted by the third-order perturbation of the gravitational potential (Krause & Hirata 2010). We also plot downward pointing cyan arrows to indicate typical angular resolutions of CMB experiments: $\ell \sim 400$ ($\theta \sim 30$ arcmin) for BICEP, Keck, and LiteBIRD; $\ell \sim 2000$ ($\theta \sim 5$ arcmin) for Planck; $\ell \sim 4000$ ($\theta \sim 3$ arcmin) for POLARBEAR and CMB-S4; $\ell \sim 10^4$ ($\theta \sim 1$ arcmin) for SPT and ACT. The bottom panel shows the ratio of simulation results to the CAMB output. The simulation results show an enhancement at very large scales, $\ell \lesssim 20$, and a small suppression at intermediate scales, $30 \lesssim \ell \lesssim 200$, arising from the lens-shell thickness, as also seen in Figure 5. The large-scale enhancement can reach 30%(70%) at $\ell = 10(2)$. The discrepancies between the simulation and CAMB are well fitted by including the lens-shell thickness effect²⁰ (the dashed red curve). For smaller scales, $\ell \gtrsim 3000$, the simulation results gradually deviate from the theoretical predictions owing to the lack of the angular resolution. For the much smaller scales of $\ell \sim 10^4$, the simulation results show an increase as a result of the shot noise. Because the particle number density decreases at higher redshift in our simulation-box configuration (see Table 1), the shot noise becomes more significant at higher source redshifts. We also numerically checked that the deflection-angle power spectrum satisfies the relations $C_\ell^d = 4C_\ell^\kappa / [\ell(\ell + 1)]$ for the gradient mode and $C_\ell^d = 4C_\ell^\omega / [\ell(\ell + 1)]$ for the curl mode (here C_ℓ^ω is the angular power spectrum of the rotation, and we compare the simulation results with theoretical predictions for C_ℓ^ω in Appendix C). The curl-mode power spectrum agrees with the leading-order post-Born correction at $\ell < 1000$. These results indicate that as predicted by Saga et al. (2015), the contributions of the vector and tensor perturbations from the nonlinear density fluctuations are negligible compared to those from the post-Born corrections at $\ell < 1000$.

We next examine the angular power spectra of CMB anisotropies. We calculated the power spectra of the temperature (T) and polarization (E/B-mode) from the 108 CMB maps. Figure 11 plots the results for TT, TE, EE, and BB in the left to right panels, respectively, as a function of ℓ . The blue and green curves show the mean values calculated from the 108 realizations. The solid red

²⁰ Here, we replaced the matter power spectrum in CAMB, as in Equation (B7).

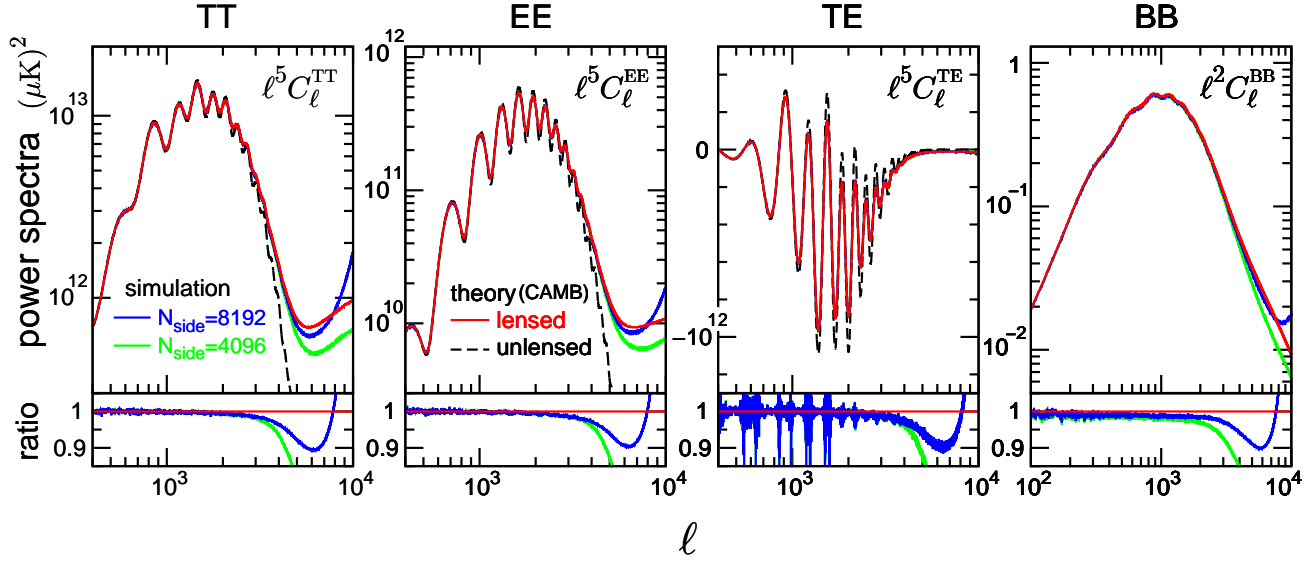


FIG. 11.— Angular power spectra of CMB temperature (T) and polarization (E/B-mode) anisotropies, given as TT, TE, EE, and BB from left to right. The y -axes give $\ell^5 C_\ell$ ($\ell^2 C_\ell$) for the TT, TE, and EE (BB) to show the results clearly. The blue and green curves give the averages from the 108 CMB maps. The solid red (dashed black) curves show the theoretical prediction of CAMB for the lensed (unlensed) case. The bottom panels show the ratios to the solid red curves.

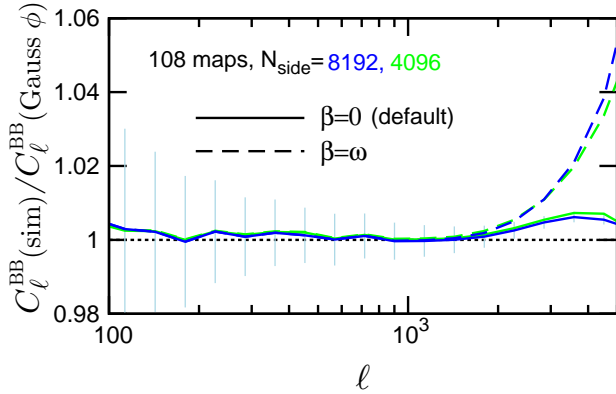


FIG. 12.— Ratio of the CMB B-mode power spectra from our simulation $C_\ell^{\text{BB}}(\text{sim})$ to that based on the Gaussian lensing potential using the Born approximation $C_\ell^{\text{BB}}(\text{Gauss } \phi)$. The power spectra are averages from the 108 maps. The results are binned with $\Delta \log_{10} \ell = 0.1$. The blue and green curves correspond to $N_{\text{side}} = 8192$ and 4096, respectively. The solid curves assume $\beta = 0$ in Equation (2), while the dashed curves assume $\beta = \omega$.

(black dashed) curves give the lensed (unlensed) power spectra calculated by CAMB. The simulation results are suppressed at small scales ($\ell \gtrsim 10^3$) owing to the lack of angular resolution and rise again at very small scales ($\ell \gtrsim 5 \times 10^3$) as a result of the shot noise. The effect of lens-shell thickness does not seem to appear in the CMB lensing because the shell-thickness influences the deflection-angle power spectrum at large scales $\ell < 200$, but the lensing effect on the CMB is not significant at such large scales. The bottom panels show the ratios to the theoretical model (CAMB) results. The ratio for C_ℓ^{TE} seems noisy because C_ℓ^{TE} crosses zero at several multipoles and the ratio diverges there. Our simulation

results agree with the theoretical prediction within 5% for $\ell < 4000$ (2000) for $N_{\text{side}} = 8192$ (4096).

To evaluate the contribution of the curl mode to the B-mode spectrum, we compared the B-mode spectrum derived above with results of a CMB map simulation in which the lensing potential, ϕ , was generated as a random Gaussian field. Note again that the lensed CMB maps based on the Gaussian lensing potential with the Born approximation do not contain the curl mode. We prepared the CMB maps as follows: (1) we first measured the average convergence power spectrum C_ℓ^κ at $z_s = 1100$ from the 108 maps and obtained the angular power spectrum of the lensing potential using the relation $C_\ell^\phi = 4C_\ell^\kappa / [\ell(\ell + 1)]^2$; (2) we generated the deflection-angle field on the sphere based on C_ℓ^ϕ assuming Gaussian fluctuations and then created the lensed CMB maps from the unlensed maps using `LenSpix` (as in Section 2.4). We prepared 108 CMB maps in this manner.

Figure 12 shows the ratio of the B-mode power spectrum in our simulation $C_\ell^{\text{BB}}(\text{sim})$ to the spectrum based on the Gaussian lensing potential $C_\ell^{\text{BB}}(\text{Gauss } \phi)$. Each curve represents a mean and error calculated from the 108 maps. The solid curves assume $\beta = 0$ (which is our default) in Equation (2), while the dashed curves assume $\beta = \omega$. As shown by the solid curves, the post-Born deflection angle enhances the B-mode power spectrum by 0.5–1% at very small scales $\ell \gtrsim 2000$. The dashed curves show stronger enhancement than the solid curves, indicating that the polarization rotation leads to the further E-to-B leakage, which is consistent with a recent analytical calculation (Marozzi et al. 2016, Figure 2) and a numerical ray-tracing simulation (Fabbian et al. 2017, Figure 17). The future CMB-S4 experiment will detect this tiny effect (Fabbian et al. 2017). In the TT, TE, and EE power spectra, the enhancements are smaller than 0.1% (1%) at $\ell < 5000$ for $\beta = 0$ ($\beta = \omega$). As the B-mode is fully generated by lensing (here we ignore any primordial B-modes), the curl mode is more prominent in C_ℓ^{BB} than

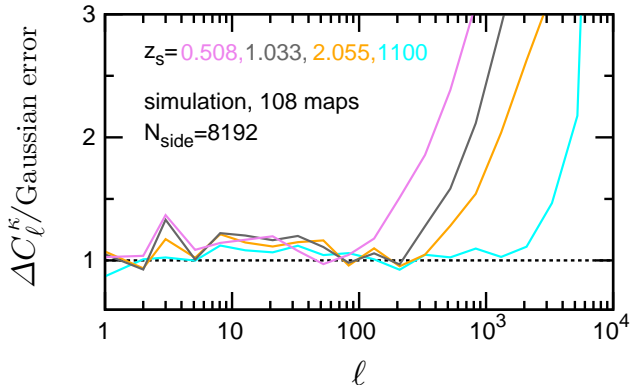


FIG. 13.— Standard deviation of C_ℓ^κ normalized by the Gaussian error for $z_s = 0.508, 1.033, 2.055, 1100$. The variance is calculated from the 108 maps with a bin width of $\Delta \log_{10} \ell = 0.2$.

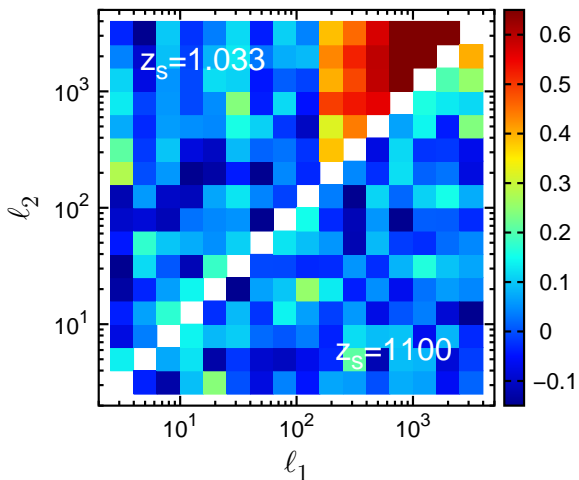


FIG. 14.— Contour plot of the correlation matrix of the convergence power spectrum calculated from the 108 maps. The upper left part corresponds to $z_s = 1.033$, while the lower right part corresponds to $z_s = 1100$. The result is for $N_{\text{side}} = 8192$ with a bin width of $\Delta \log_{10} \ell = 0.2$.

in the other CMB power spectra.

4. COVARIANCES OF OBSERVABLES

In this section, we calculate the covariances of the convergence power spectrum (Section 4.1) and the CMB B-mode power spectrum (Section 4.2). We then compare these to a simple Gaussian variance. We also discuss variances in regions taken from the all-sky maps for the shear correlation functions and halo-galaxy lensing (Section 4.3). We ignore the shape noise for these analyses.

4.1. Covariance of the Convergence Power Spectrum

We evaluate the covariance of the convergence power spectrum C_ℓ^κ from the 108 simulation maps with the main goal of checking the independence of the maps. Because we constructed the 108 maps from the 84 N -body realizations, the maps are not strictly indepen-

dent. The covariance of C_ℓ^κ can be written as (e.g., Meiksin & White 1999; Scoccimarro et al. 1999)

$$\begin{aligned} \text{cov}(\ell_1, \ell_2) &\equiv \langle (C_{\ell_1}^\kappa - \langle C_{\ell_1}^\kappa \rangle) (C_{\ell_2}^\kappa - \langle C_{\ell_2}^\kappa \rangle) \rangle \\ &= \frac{2}{N_{\ell_1}} (C_{\ell_1}^\kappa)^2 \delta_{\ell_1 \ell_2} + T_{\ell_1 \ell_2}. \end{aligned} \quad (17)$$

The first term gives the Gaussian variance, $N_\ell (= 2\pi\ell\Delta\ell)$ is the number of modes between ℓ and $\ell + \Delta\ell$, and $\delta_{\ell_1 \ell_2}$ is the Kronecker delta. The second term, written by the trispectrum, is the non-Gaussian contribution arising from mode coupling during nonlinear gravitational evolution.

Figure 13 shows the standard deviation of C_ℓ^κ normalized by the Gaussian error (the square root of the first term in Equation (17)) with the source redshifts $z_s = 0.508, 1.033, 2.055, 1100$ at $N_{\text{side}} = 8192$. Here, we use the average C_ℓ^κ measured from the simulation maps to calculate the Gaussian variance. The power spectrum is binned with the width $\Delta \log_{10} \ell = 0.2$. The figure clearly shows that the errors are consistent with the Gaussian error for large scales ($\ell < 100$), which suggest that the maps can be treated as independent²¹. The non-Gaussian error is more significant at smaller scales ($\ell > 100$), especially for lower source redshift. Note that because only the Gaussian error depends on the bin width in Equation (17), the relative importance of the non-Gaussian term is less significant at smaller bin-widths. Finally, we note that according to previous studies (e.g., Hartlap et al. 2007; Taylor et al. 2013), the typical accuracy of the variance estimated from the 108 samples is $(108/2)^{-1/2} \sim 14\%$. The scatter seen in the figure at $\ell < 100$ is roughly consistent with this estimate and thus is caused by the finite number of samples.

We next examine the off-diagonal elements of the covariance matrix. Here, we define the correlation matrix as

$$\text{corr}(\ell_1, \ell_2) = \frac{\text{cov}(\ell_1, \ell_2)}{\sqrt{\text{cov}(\ell_1, \ell_1) \text{cov}(\ell_2, \ell_2)}}. \quad (18)$$

The diagonal elements of this matrix are always unity by definition, while the off-diagonal elements measure the relative strength of correlation between different multipoles. Figure 14 shows a contour plot of the correlation matrix. The top left (bottom right) triangle corresponds to $z_s = 1.033$ (1100). As seen in the figure, the correlation is very weak at large scales ($\ell < 100$) at both redshifts; however, a strong correlation is seen at smaller scales ($\ell \gtrsim 200$) at $z_s = 1.033$.

Petri et al. (2016a) recently demonstrated that one or two N -body realizations are sufficient to construct $\sim 10^4$ independent weak-lensing maps based on an investigation of the numerical convergence of the covariances of the convergence power spectrum and peak count by varying the number of N -body simulations. In their Figure 3, there does not seem to be a correlation between the number of N -body simulations and the amplitude of the C_ℓ^κ variance. For instance, the smaller N -body realiza-

²¹ However, the variance seems $\sim 20\%$ larger than the Gaussian prediction at $\ell = 1 - 100$, which might be caused by the finite shell-thickness effect. This effect slightly changes the convergence power spectrum at $\ell \lesssim 100$ (see Section 3.1) and thus may also affect its covariance at such large scales.

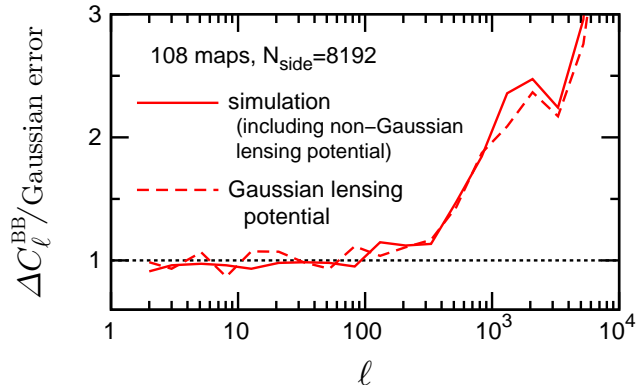


FIG. 15.— Standard deviation of the CMB B-mode power spectrum normalized by Gaussian error. The variance is calculated from the 108 maps. The solid curve is calculated from the simulation maps (including the non-Gaussian lensing potential), while the dashed curve is calculated from the maps based on the Gaussian lensing potential with the Born approximation. Here, we set $N_{\text{side}} = 8192$ with a bin width of $\Delta \log_{10} \ell = 0.2$.

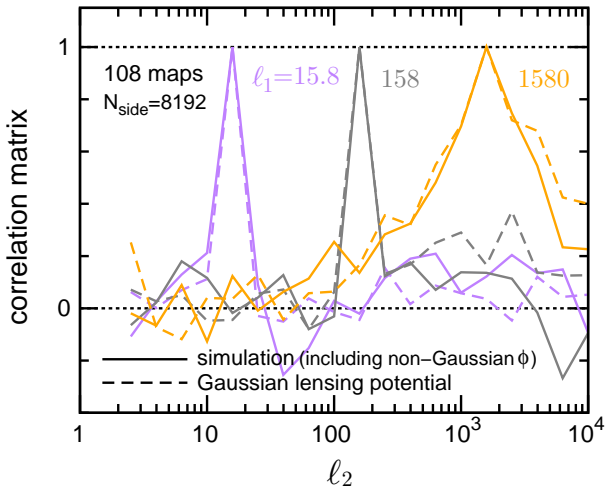


FIG. 16.— Correlation matrix of the CMB B-mode power spectrum calculated from the 108 maps as a function of ℓ_2 with $\ell_1 = 15.8$ (purple), 158 (gray), and 1580 (orange), respectively. The solid curves are calculated from the simulation maps (including the non-Gaussian lensing potential ϕ), while the dashed curves are from the maps based on the Gaussian lensing potential. The result corresponds to $N_{\text{side}} = 8192$ with a bin width of $\Delta \log_{10} \ell = 0.2$.

tions tend not to generate the smaller (or larger) variance. According to their results, our 84 simulations are large enough to construct independent maps.

4.2. Covariance of the CMB B-mode Power Spectrum

We next calculate the covariance of the CMB B-mode power spectrum. As the B-mode is fully generated by gravitational lensing, it contains more non-Gaussianity than either the temperature or E-mode polarization (e.g., Benoit-Levy et al. 2012). This non-Gaussianity increases the sampling error in the B-mode power spectrum and makes the B-mode less sensitive to cosmology.

Figure 15 plots the standard deviation of the CMB

B-mode power spectrum C_ℓ^{BB} calculated from the 108 maps. The solid curve corresponds to $C_\ell^{\text{BB}}(\text{sim})$ measured in our simulation, while the dashed curve corresponds to $C_\ell^{\text{BB}}(\text{Gauss } \phi)$ based on the Gaussian lensing potential with the Born approximation described in Section 3.5. To calculate the Gaussian variance in the denominator, we used the average C_ℓ^{BB} for each case. As seen in Figure 15, the two curves agree well up to $\ell = 5000$, suggesting that the lowest-order lensing deflection is the main source of the non-Gaussianity and the multiple-scattering does not make a strong contribution.

Figure 16 plots the correlation matrix as a function of ℓ_2 for various multipole values, $\ell_1 = 15.8, 158,$ and 1580 . As in Figure 15, the solid curves show $C_\ell^{\text{BB}}(\text{sim})$, while the dashed curves show $C_\ell^{\text{BB}}(\text{Gauss } \phi)$. As there are no clear differences between the solid and dashed curves (although there are large scatters), Figures 15 and 16 suggest that estimating the covariance of the CMB B-mode power spectrum based on the Gaussian lensing potential with the Born approximation would be valid up to $\ell \simeq 5000$. However, we note that more realizations with higher resolutions are necessary to resolve these differences clearly.

4.3. Variance Estimated from 48 Regions in the All-sky Map

In this subsection, we assess the independence of various regions taken from a single full-sky map. Owing to mode coupling during nonlinear gravitational evolution, density fluctuations in different survey regions correlate to each other. As a simple example, we took 48 equal-area regions represented by HEALPix large pixels with $N_{\text{side}} = 4$ with identical surface areas of $4\pi/48$ ($\simeq 860 \text{ deg}^2$). The angular pixel resolution in each region was also the same ($N_{\text{side}} = 4096$ or 8192). We used 96 full-sky maps to produce $4608 (= 48 \times 96)$ regions in total and calculated the variances of shear correlation functions and halo-galaxy lensing for the two following cases.

(I) *Variance in each map* We calculated the variance among 48 regions taken from a single map. In total, we used 96 estimates of variance from 96 all-sky maps.

(II) *Variance in each region* We took one out of the 48 regions from each of the 96 maps at the same sky position. We further divided these 96 maps into two groups of 48 each and computed the variance within each group to perform a straightforward comparison with case (I). We produced $96 (= 2 \times 48)$ estimates of variance in total.

Figure 17 shows the standard deviations of the shear correlation functions ξ_+^γ (left panel) and ξ_-^γ (right panel) at $z_s = 1.033$. We directly computed the shear correlations ξ_\pm^γ using all pairs in the region (i.e., using the brute-force approach). The thin light-blue and gray curves represent cases (I) and (II), respectively. The thick black and blue curves show the averages of the thin curve sets. The difference between the thick black and blue curves is smaller than 10% at $\theta > 3(4)$ arcmin for ξ_+^γ (ξ_-^γ). The blue lines are slightly larger at very small scales (close to the pixel size). The angular resolution for ξ_+ (ξ_-) at $N_{\text{side}} = 4096$ is 1 (10) arcmin (see Figure 7), indicating that the discrepancies at small scale would be owing to

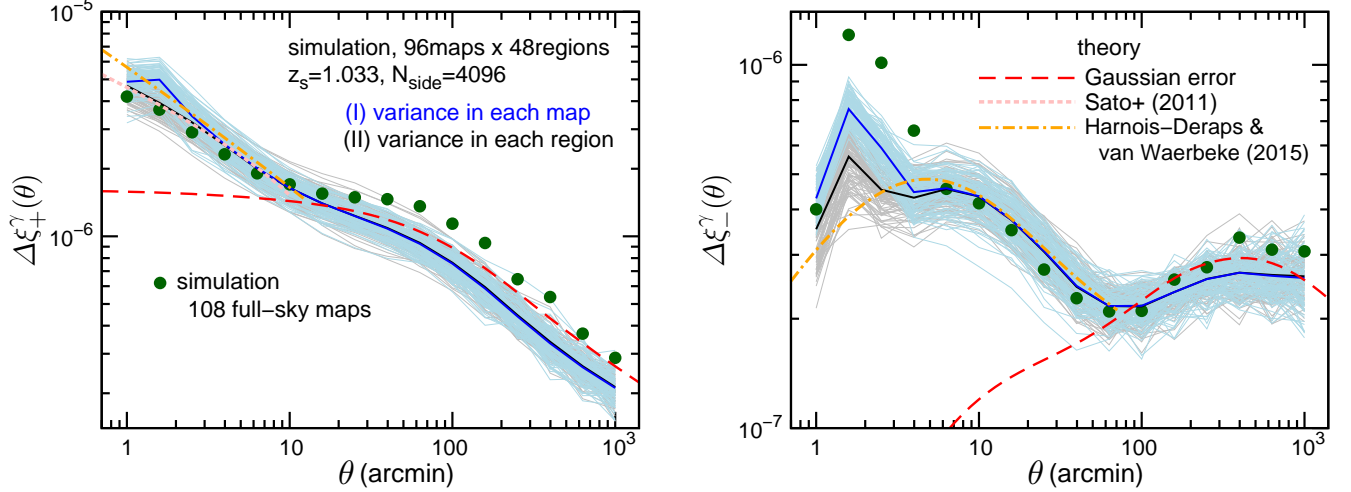


FIG. 17.— Standard deviations of the shear correlation functions at $z_s = 1.033$. The thin light-blue lines are the variances calculated using 48 regions in each all-sky map (case (I)), while the thin gray lines are calculated using 48 regions in the same sky position in the 48 maps (case (II), see also main text). The thick blue and black lines show the averages of the thin light-blue and gray line sets, respectively. The green circles are the errors measured from the 108 full-sky maps, multiplied by $\sqrt{48}$ to take into account the survey area ratio. The dashed red curves are the analytical prediction of the Gaussian error. The dotted pink and dash-dotted orange curves are the fitting formulae of the non-Gaussian error in Sato et al. (2011) and Harnois-Déraps & van Waerbeke (2015), respectively. The results are for $N_{\text{side}} = 4096$ with a bin width of $\Delta \log_{10}(\theta/\text{arcmin}) = 0.2$.

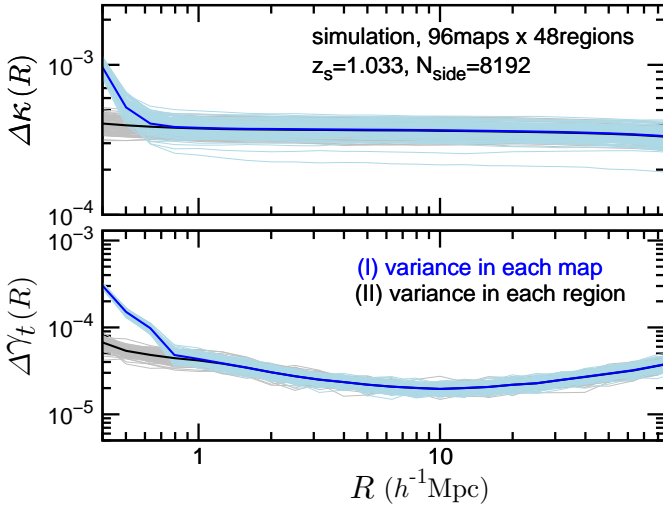


FIG. 18.— Standard deviations of the halo-galaxy lensing for sample 1 at $z_s = 1.033$. The results are the variances of the convergence profile (upper panel) and the tangential shear profile (lower panel). Here, we set $N_{\text{side}} = 8192$ with a bin width of $\Delta \log_{10}[R/(h^{-1}\text{Mpc})] = 0.1$.

the lack of angular resolution²². The green circles are the errors measured from the 108 full-sky maps. Here a factor $\sqrt{48}$ is multiplied to rescale them to take into account the differences in area. The large error seen in the right panel for $\theta < 5$ arcmin would be caused by the finite angular resolution. We also indicate the Gaussian error with the dashed red curves. The variance of the shear correlation functions for the Gaussian fluctuations

²² Owing to pixelization, the angular separations between pixels can be sampled only discretely. The impact of this discreteness is larger on small scales close to the pixel size. This effect is common in samples in which the variance is computed in case (II) (because the pixelization in the survey region is always the same) but uncommon in case (I). The difference in discreteness of the separation among the samples would cause differences in the variances at very small scales.

can be obtained from Equation (7) as (e.g., Ng & Liu 1999, Section VII)

$$\begin{aligned} \left[\Delta \xi_{\pm}^{\gamma(\text{Gauss})}(\theta) \right]^2 &\equiv \langle [\xi_{\pm}^{\gamma}(\theta) - \langle \xi_{\pm}^{\gamma}(\theta) \rangle]^2 \rangle \\ &= \frac{2}{\Omega_{\text{W}}} \sum_{\ell=2}^{\infty} \left[\left(C_{\ell}^{\gamma(\text{E})} \right)^2 + \left(C_{\ell}^{\gamma(\text{B})} \right)^2 \right] [{}_2Y_{\ell\mp 2}(\theta, 0)]^2, \end{aligned} \quad (19)$$

where $\Omega_{\text{W}} (= 4\pi/48)$ is the survey area in units of steradians. The above equation reduces to the flat-sky result in Joachimi et al. (2008) in the small-angle limit. In Equation (19), we adopt the spherical-sky formula for the E-mode $C_{\ell}^{\gamma(\text{E})}$ and ignore the B-mode $C_{\ell}^{\gamma(\text{B})}$ (as in Section 3.2). Figure 17 shows that the blue and black curves are slightly smaller (10 – 20%) than the Gaussian error (19) for larger scales. Sato et al. (2011) showed that the theoretical Gaussian error in Joachimi et al. (2008) is less accurate and overestimates the variance for a smaller survey area of $\Omega_{\text{W}} \lesssim 10^3 \text{ deg}^2$. The above discrepancies seem to be consistent with their finding. In other words, as they noted, the Gaussian error does not simply scale as $\Delta \xi_{\pm}^{\gamma(\text{Gauss})} \propto \Omega_{\text{W}}^{-1/2}$, which is also consistent with the discrepancy between the green symbols and the black (or blue) curves. The green circles are slightly larger (10 – 20%) than the Gaussian error (19) for $\theta \gtrsim 100$ arcmin, which is consistent with the small enhancement of the C_{ℓ}^{κ} variance at $\ell \lesssim 100$ seen in Fig. 13.

The non-Gaussian signature is clearly observed on the small scales, where the simulation results are well above the Gaussian estimate. We also plot the fitting formulae of the non-Gaussian error given by Sato et al. (2011) and Harnois-Déraps & van Waerbeke (2015) (see also Semboloni et al. 2007, for an earlier fitting formula). They measured the covariance matrix of ξ_{\pm}^{γ} from ensembles of weak-lensing maps based on ray-tracing simulation. According to their work, the non-Gaussian error is a product of a fitting function $F_{\pm}(\theta)$ and the Gaussian

error defined in Equation (19)

$$[\Delta\xi_{\pm}^{\gamma}(\theta)]^2 = F_{\pm}(\theta) \left[\Delta\xi_{\pm(\text{Gauss})}^{\gamma}(\theta) \right]^2, \quad (20)$$

where $F_{\pm}(\theta)$ approaches unity for large θ . The dotted pink and dash-dotted orange curves in Figure 17 correspond to their fitting formulae (the dotted pink curve is only for $\Delta\xi_{+}$). Here we plot them only for $F_{\pm}(\theta) > 1$. These curves agree well with the simulation results.

Figure 18 shows the standard deviations for halo-galaxy lensing for sample 1 (Table 3). The upper and lower panels show the convergence and tangential shear profiles, respectively. Here the halos were within each region, but the background fields ($\kappa, \gamma_{1,2}$) were taken from the all-sky sample (including outside the region). The blue and black curves agree at $R > 0.6$ (0.8) $h^{-1}\text{Mpc}$ for the convergence (the tangential shear) profile, but the blue curves are larger at small scales. These features are the same as in the shear correlation function shown in Figure 17. The discrepancies at small scales are caused by the lack of angular resolution (which corresponds to $R \sim 1 h^{-1}\text{Mpc}$ in Figure 8).

In summary, we can consider the 48 regions taken from the all-sky map to be independent samples in terms of cosmic shear and halo-galaxy lensing. We note that the density fluctuations approach Gaussian for a higher redshift or larger survey area, in which cases the correlations between the different regions would be smaller.

5. KNOWN ISSUES

We note that our all-sky maps have small anomalies: (i) the convergence at low source redshift ($z_s < 0.3$) can be smaller than the minimum value expected for the empty beam (which is given by setting $\delta = -1$ in Equation (3)), and; (ii) the amplitudes of the shear B-mode are slightly larger than theoretical predictions. Feature (i) appears more frequently for lower source redshifts, and feature (ii) is probably the result of a numerical error that is caused by the finite angular resolution. We note that these anomalies are negligibly small for most practical purposes. A detailed discussion of the anomalies is given in Appendix C.

As shown in Section 3, the lens-shell thickness effect somewhat degrades the accuracy of our mocks. For instance, the shear correlation functions (or power spectra) decrease by at most 5% – 10% at intermediate scales $\theta = 10 - 10^3$ arcmin (or $\ell = 10 - 100$). Similarly, for the CMB lensing, the deflection-angle power spectrum increases up to 70% at very small scales $\ell = 2 - 10$, which might be a problem for a reconstruction of the full-sky lensing potential.

The shot noise, caused by the low number density of dark matter particles, is more significant for higher source redshifts (see Table 2) and therefore especially for CMB lensing. We note that the shot noise depends on the sky direction in our simulation setting. The dark matter particles are placed on grids in the simulation box at the initial redshift, but do not move significantly from their initial positions at high redshifts. Therefore, projecting the particles onto the lens shells causes them to align along the x -, y -, or z -axis, resulting in noisy patterns on the spheres along arcs of $\theta = \pi/2$, $\phi = 0$, $\pi/2$, π , and $3\pi/2$. This effect can be avoided if the particles are not distributed on grids in the initial redshift

(for example, the so-called glass initial condition; see, e.g., Wang & White 2007). An example can be found in the middle rectangular panel of Figure 4, in which a noisy pattern is apparent. Shot noise features are significant for the convergence power spectrum, but not for the deflection angle at $z_s = 1100$ because the convergence (deflection angle) is the second (first) derivative of the lensing potential and therefore is more (less) sensitive to density contrast at the small scales close to the pixel size.

We should also comment on the effects of baryons and neutrinos on the simulation (our simulation only includes dark matter). Owing to baryon cooling, baryons strongly enhance matter clustering at small scales, but they suppress clustering at intermediate scales owing to feedback from active galactic nuclei (AGN), supernovae, and stellar winds (e.g., van Daalen et al. 2011; Vogelsberger et al. 2014b). For instance, baryons enhance the matter power spectrum by an order of magnitude at $k \gtrsim 100 h\text{Mpc}^{-1}$ but suppress it by a few tens of a percent at $k \approx 10 h\text{Mpc}^{-1}$. AGN feedback also suppresses the number density of halos by a few tens of a percent at $M \gtrsim 10^{14} M_{\odot}$ (Vogelsberger et al. 2014a). Current and future weak-lensing surveys will detect such baryonic effects via the shear correlation functions, convergence peak counts, or Minkowski functionals (e.g., Semboloni et al. 2011; Harnois-Déraps et al. 2015; Osato et al. 2015). These baryonic effects on the matter power spectrum can be taken into account using the fitting formula given by Harnois-Déraps et al. (2015). Massive neutrinos also suppress the matter power spectrum at $k \gtrsim 0.1 h\text{Mpc}^{-1}$ as a result of free streaming, and future CMB experiments will measure neutrino streaming through the CMB lensing and constrain the neutrino mass (e.g., CMB-S4 Collaboration 2016).

6. SUMMARY AND DISCUSSION

We presented 108 full-sky weak-lensing maps constructed using a multiple-lens ray-tracing technique through cosmological N -body simulations. The full numerical simulation included nonlinear gravitational evolution, non-Gaussian error, collapsed objects (i.e., halos), and the post-Born corrections. The resulting maps contain convergence, shear, and rotation fields at $z_s = 0.05 - 5.3$ and CMB temperature and polarization fields at $z_s = 1100$. These maps were prepared for every $150 h^{-1}\text{Mpc}$ comoving distance (corresponding to a redshift interval of $\Delta z \simeq 0.05$ near $z = 0$), thereby enabling the construction of a realistic shear map for an arbitrary source distribution. The simulation has sufficient mass resolution to resolve the host halos of the SDSS CMASS galaxies and LRGs. We demonstrated in Section 3 that the simulation results agree closely with theoretical predictions for cosmic shear, halo-galaxy lensing, halo clustering, and CMB lensing. In Section 4 we confirmed the mutual independence of the 108 maps, and furthermore showed that regions taken from the all-sky maps are effectively independent as well. Thus, these mocks can be safely used to estimate the covariances of observables or test an analysis tool for real observational data. The maps are freely available for download at the website²³,

²³ http://cosmo.phys.hirosaki-u.ac.jp/takahasi/allsky_raytracing/

where we provide a user's guide (which is also included in Appendix D).

Combining different observational probes enables breaking cosmological parameter degeneracies and therefore provides stronger constraints on the cosmological parameters. For instance, although there are currently several distinct probes including cosmic shear, galaxy-galaxy lensing, galaxy clustering, cluster abundance, and CMB lensing, the cosmological constraints inferred from these probes are not independent, but rather are correlated because they trace the same underlying mass distribution. In this situation, our mocks are quite useful for estimating the cross covariances between different observables in the cosmological likelihood analysis.

The 108 full-sky maps are the largest data sets so far, but they are not large enough to estimate the covariances of observables in some cases, such as for cross-correlation analyses and higher-order (three- or four-point) correlation analyses for large survey areas. In such cases, the estimated covariance will be noisy because the number of data sets is very large. Recently, Murata et al. (2017) used the 108 catalogs to estimate the covariance of cluster-galaxy lensing for the redMaPPer clusters. They measured the jackknife covariance in each map and then calculated the average from the 108 maps to reduce the noisy feature.

Finally, we would like to note some related work that uses our mock catalogs. Shirasaki et al. (2017) recently discussed the covariances of cluster/galaxy-galaxy lensing for the SDSS LRG, CMASS, and redMaPPer clusters using our first 48 maps and then compared the result to

the jackknife covariance. Higuchi & Inoue (2017) investigated the detectability of a supervoid via weak lensing of background galaxies. The HSC science analyses are also currently using the catalogs in their likelihood analysis (e.g., Mandelbaum et al. 2017; Oguri et al. 2017). In these papers, the simulation and the observational data agree well, and they show how well our mocks serve their purposes.

We would like to thank Eric Hivon, Matthias Bartelmann, Masamune Oguri, Yuji Chinone, Joachim Harnois-Déraps, Antony Lewis, and Giovanni Marozzi for their useful comments and discussion. We would like to thank M. R. Becker for making the source program of CALCLENS available, and the HEALPix team for making the HEALPix software publicly available. This work was supported in part by JSPS KAKENHI Grant No. JP17H01131 (R.T.) and MEXT KAKENHI Grant Number 26400285 (T.H.), 17K05457 (T.H.) and 17K14273 (T.N.). This work is in part supported by MEXT Grant-in-Aid for Scientific Research on Innovative Areas (Nos. 15H05887, 15H05892, and 15H05893). M.S. is supported by Research Fellowships of the Japan Society for the Promotion of Science (JSPS) for Young Scientists. T.N. acknowledges financial support from Japan Science and Technology Agency (JST) CREST Grant Number JP-MJCR1414. Numerical computations presented in this paper were in part carried out on Cray XC30 and on the general-purpose PC farm at Center for Computational Astrophysics, CfCA, of the National Astronomical Observatory of Japan.

REFERENCES

- ACTPol Collaboration (Sherwin, B., van Engelen, A., Sehgal, N. et al.) 2017, arXiv:1611.09753
- Aihara, H., Armstrong, R., Bickerton, S. et al. 2017, arXiv:1702.08449, submitted to PASJ
- Alam, S., Albareti, F.D., Allende Prieto, C. et al., 2015, ApJS, 219, 12
- Baltz, E.A., Marshall, P. & Oguri, M. 2009, JCAP, 01, 015
- Bartelmann, M. & Schneider, P., 2001, Phys. Rep., 340, 291
- Bartelmann, M. & Maturi, M. 2016, arXiv:1612.06535
- Becker, M.R. 2013, MNRAS, 435, 115
- Behroozi, P.S., Wechsler, R.H., & Wu, H.-Y., 2013, ApJ, 762, 109
- Benoit-Lévy, A., Smith, K., & Hu, W., 2012, Phys. Rev. D, 86, 123008
- BICEP2/Keck Array Collaborations, 2016, ApJ, 833, 228
- Boehm, V., Schmittfull, M. & Sherwin, B. 2016, Phys. Rev. D, 4, 043519
- Carbone, C., Springel, V., Baccigalupi, C., et al. 2008, MNRAS, 388, 1618
- Carbone, C., Baccigalupi, C., Bartelmann, M., et al. 2009, MNRAS, 396, 668
- Challinor, A., & Lewis, A., 2005, Phys. Rev. D, 71, 103010
- Chang, C., Jarvis, M., Jain, et al. B. 2013, MNRAS, 434, 2121
- CMB-S4 Collaboration, 2016, arXiv:1610.02743
- Cooray, A. & Hu, W., 2001, ApJ, 554, 56
- Cooray, A. & Hu, W., 2002, ApJ, 574, 19
- Cooray, A. & Sheth, R. 2002, Physics Reports, 372, 1
- Crocce, M., Pueblas, S., & Scoccimarro, R., 2006, MNRAS, 373, 369
- Dark Energy Survey Collaboration 2016a, MNRAS, 460, 1270
- Dark Energy Survey Collaboration 2016b, Phys. Rev. D, 94, 022001
- Das, S. & Ostriker, J.P., 2006, ApJ, 645, 1
- Das, S. & Bode, P. 2008, ApJ, 682, 1
- de Jong, J.T.A., Verdoes Kleijn, G.A., Boxhoorn, D.R. 2015, A&A, 582, A62
- Dodelson, S. 2003, Modern Cosmology (New York: Academic Press)
- Duffy, A.R., Schaye, J., Kay, S.T., & Dalla Vecchia, C. 2008, MNRAS, 390, L64
- Eisenstein, D.J., Annis, J., Gunn, J.E., et al. 2001, ApJ, 122, 2267
- Fabbian, G., Calabrese, M., & Carbone, C. 2017, arXiv:1702.03317, submitted to JCAP
- Fosalba, P., Gaztañaga, E., Castander, F.J., & Manera, M. 2008, MNRAS, 391, 435
- Fosalba, P., Crocce, M., Gaztañaga, E., & Castander, F.J., 2015a, MNRAS, 448, 2987
- Fosalba, P., Gaztañaga, E., Castander, F.J., & Crocce, M. 2015b, MNRAS, 447, 1319
- Giannantonio, T., Fosalba, P., Cawthon, R., et al. 2016, MNRAS, 456, 3213
- Górski, K.M., Hivon, E., Banday, A.J. et al. 2005, ApJ, 622, 759
- Hamana, T., Martel, H., & Futamase, T. 2000, ApJ, 529, 56
- Hamana, T. & Mellier, Y. 2001, MNRAS, 327, 169
- Hamana, T., Sakurai, J., Koike, M., & Miller, L. 2015, PASJ, 67, 34
- Hamilton, A.J.S. 2000, MNRAS, 312, 257
- Harnois-Déraps, J., Vafaei, S., & van Waerbeke, L. 2012, MNRAS, 426, 1262
- Harnois-Déraps, J., van Waerbeke, L., Viola, M., & Heymans, C. 2015, MNRAS, 450, 1212
- Harnois-Déraps, J. & van Waerbeke, L. 2015, MNRAS, 450, 2857
- Hartlap, J., Simon, P., & Schneider, P. 2007, A&A, 464, 399
- Heitmann, K., Higdon, D., White, M., et al. 2009 ApJ, 705, 156
- Heitmann, K., White, M., Wagner, C., et al. 2010, ApJ, 715, 104
- Heitmann, K., Bingham, D., Lawrence, E., et al. 2016, ApJ, 820, 108
- Heymans, C., van Waerbeke, L., Miller, L. et al. 2012, MNRAS, 427, 146
- Heymans, C., Groot, E., Heavens, A. et al. 2013, MNRAS, 432, 2433

- Higuchi, Y. & Inoue, K. T. 2017, arXiv:1707.07535, submitted to MNRAS
- Hilbert, S., White, S.D.M., Hartlap, J., & Schneider, P. 2007, MNRAS, 382, 121
- Hilbert, S., Hartlap, J., White, S.D.M., & Schneider, P. 2009, A&A, 499, 31
- Hildebrandt, H., Viola, M., Heymans, C., et al. 2017, MNRAS, 465, 1454
- Hinshaw, G., Larson, D., Komatsu, E., 2013, ApJS, 208, 19
- Hirata, C.M. & Seljak, U. 2003, Phys. Rev. D, 68, 083002
- Hirata, C.M., Ho, S., Padmanabhan, N., et al. 2008, Phys. Rev. D, 78, 043520
- Hoekstra, H. & Jain, B. 2008, Annual Review of Nuclear and Particle Science, 58, 99
- Hu, W. & White, M. 1997, Phys. Rev. D, 56, 596
- Hu, W. 2000, Phys. Rev. D, 62, 043007
- Jain, B., Seljak, U., & White, S. 2000, ApJ, 530, 547
- Joachimi, B., Schneider, P., Eifler, T. 2008, A&A, 477, 43
- Kaiser, N. 1992, ApJ, 388, 272
- Kayo, I., Takada, M. & Jain, B. 2013, MNRAS, 429, 344
- Kamionkowski, M., Kosowsky, A., & Stebbins, A. 1997, Phys. Rev. D, 55, 7368
- Kesden, M., Cooray, A. & Kamionkowski, M., 2002, Phys. Rev. Lett., 89, 011304
- Kiessling, A., Heavens, A.F., Taylor, A.N., & Joachimi, B. 2011, MNRAS, 414, 2235
- Kilbinger, M., Fu, L., Heymans, C., Simpson, F. 2013, MNRAS, 430, 2200
- Kilbinger, M. 2015, Rep. Prog. Phys., 78, 086901
- Kilbinger, M., Heymans, C., Asgari, M., et al., 2017, submitted to MNRAS, arXiv:1702.05301
- Kitching, T.D., Alsing, J., Heavens, A.F., et al., 2017, MNRAS, 469, 2737
- Knox, L., & Song, Y.-S. 2002, Phys. Rev. Lett., 89, 011303
- Krause, E. & Hirata, C.M. 2010, A&A, 523, A28
- Lawrence, E., Heitmann, K., White, M. et al., 2010, ApJ, 713, 1322
- Lewis, A., Challinor, A. & Lasenby, A., 2000, ApJ, 538, 473
- Lewis, A. & Challinor, A. 2006, Physics Reports, 429, 1
- Lewis, A., Hall, A., Challinor, A. 2017, JCAP, 08, 23
- Liu, J., Hill, C., Sherwin, B., Petri, A., Boehm, V., & Haiman, Z. 2016, Phys. Rev. D, 10, 103501
- Mandelbaum, R., Slosar, A., Baldauf, T. et al., 2013, MNRAS, 432, 1544
- Mandelbaum, R., Miyatake, H., Hamana, T. et al. 2017, arXiv:1705.06745, submitted to PASJ
- Marozzi, G., Fanizza, G., Di Dio, E., & Durrer, R. 2016, arXiv:1612.07263
- Meiksin, A. & White, M. 1999, MNRAS, 308, 1179
- Miyatake, H., More, S., Mandelbaum, R., et al. 2015, ApJ, 806, 1
- Miyatake, H., More, S., Takada, M., et al. 2016a, Phys. Rev. Lett., 118, 161301
- Miyatake, H., Madhavacheril, M.S., Sehgal, N., et al. 2016b, Phys. Rev. Lett., 116, 041301
- Miyazaki, S., Komiyama, Y., Nakaya, H., et al. 2012, Proc. SPIE, 8446, 84460Z
- Munshi, D., Valageas, P., van Waerbeke, L., & Heavens, A. 2008, Phys. Rep., 462, 67
- Murata, R., Nishimichi, T., Takada, M., et al. 2017, arXiv:1707.01907, submitted to ApJ
- Namikawa, T., 2016, Phys. Rev. D, 93, 121301
- Namikawa, T., Yamauchi, D. & Taruya, A. 2012, JACP, 12, 007
- Navarro, J.F., Frenk, C.S. & White, S.D.M. 1997, ApJ, 490, 493
- Ng, K.-W. & Liu, G.-C. 1999, Int. J. Mod. Phys. D, 8, 61
- Nishimichi, T., Shirata, A., Taruya, A., et al., 2009, PASJ, 61, 321
- Oguri, M. & Takada, M. 2011, Phys. Rev. D, 83, 023008
- Oguri, M. & Hamana, T. 2011, MNRAS, 414, 1851
- Oguri, M., Miyazaki, S. & Hikage, C., et al. 2017, arXiv:1705.06792, submitted to PASJ
- Omori, Y., Chown, R., Simard, G., et al. 2017, arXiv:1705.00743
- Osato, K., Shirasaki, M., & Yoshida, N. 2015, ApJ, 806, 186
- Petri, A., Haiman, Z., & May, M. 2016a, Phys. Rev. D, 93, 063524
- Petri, A., May, M. & Haiman, Z. 2016b, Phys. Rev. D, 94, 063534
- Planck Collaboration 2016a, A&A, 594, A13
- Planck Collaboration 2016b, A&A, 594, A15
- POLARBEAR Collaboration 2014, Phys. Rev. Lett., 113, 021301
- Pratten, G. & Lewis, A. 2016, JCAP, 08, 047
- Reid, B.A., Percival, W.J., Eisenstein, D.J., et al. 2010, MNRAS, 404, 60
- Rykoff, E.S., Rozo, E., Busha, M.T., et al. 2014, ApJ, 785, 104
- Saga, S., Yamauchi, D., Ichiki, K., 2015, Phys. Rev. D, 92, 063533
- Sato, M., Hamana, T., Takahashi, R., Takada, M. et al. 2009, ApJ, 701, 945
- Sato, M., Takada, M., Hamana, T., & Matsubara, T. 2011, ApJ, 734, 76
- Sato, M. & Nishimichi, T. 2013, Phys. Rev. D, 87, 123538
- Schneider, P., van Waerbeke, L., Kilbinger, M. & Mellier, Y. 2002, A&A, 396, 1
- Schneider, P., Kochanek, C., & Wambsganss, J. 2006, Gravitational Lensing: Strong, Weak and Micro (Springer-Verlag, Berlin, Heidelberg, 2006)
- Soccimarro, R., Zaldarriaga, M., & Hui, L. 1999, ApJ, 527, 1
- Sehgal, N., Bode, P., Das, S. 2010, ApJ, 709, 920
- Seljak, U., Makarov, A., Mandelbaum, R., Hirata, C.M. 2005, Phys. Rev. D, 71, 043511
- Semboloni, E., van Waerbeke, L., Heymans, C., et al. 2007, MNRAS, 375, L6
- Semboloni, E., Hoekstra, H., Schaye, J., et al. 2011, MNRAS, 417, 2020
- Shirasaki, M., Hamana, T., & Yoshida, N. 2015, MNRAS, 453, 3043
- Shirasaki, M., Takada, M., Miyatake, H., et al. 2017, MNRAS, 470, 3476
- Shirasaki, M. 2017, MNRAS, 465, 1974
- Singh, S., Mandelbaum, R., & Brownstein, J.R. 2017, MNRAS, 464, 2120
- Smith, R.E., Peacock, J.A., Jenkins, A., et al. 2003, MNRAS, 341, 1311
- Smith, K.M., Zahn, O., & Doré, O. 2007, Phys. Rev. D, 76, 043510
- SPTpol Collaboration (Story, K., Hanson, D., et al.), 2014, ApJ, 810, 50
- Springel, V., Yoshida, N. & White, S.D.M., 2001, New Astronomy, 6, 79
- Springel, V., 2005, MNRAS, 364, 1105
- Stebbins, A., 1996, submitted to ApJ, astro-ph/9609149
- Takada, M. & Hu, W. 2013, Phys. Rev. D, 87, 123504
- Takahashi, R., Yoshida, N., Takada, M. et al. 2009, ApJ, 700, 479
- Takahashi, R., Oguri, M., Sato, M., & Hamana, T. 2011, ApJ, 742, 15
- Takahashi, R., Sato, M., Nishimichi, T., Taruya, A., & Oguri, M. 2012, ApJ, 761, 152
- Taruya, A., Takada, M., Hamana, T. et al. 2002, ApJ, 571, 638
- Taylor, A., Joachimi, B., & Kitching, T. 2013, MNRAS, 432, 1928
- Teyssier, R., Pires, S., Prunet, S., et al. 2009, A&A, 497, 335
- Tinker, J., Kravtsov, A.V., Klypin, A., et al. 2008, ApJ, 688, 709
- Tinker, J.L., Robertson, B.E., Kravtsov, A.V., et al. 2010, ApJ, 724, 878
- Vale, C. & White, M. 2003, ApJ, 592, 699
- van Daalen, M.P., Schaye, J., Booth, C.M., & Vecchia, C.D. 2011, MNRAS, 415, 3649
- van Engelen, A., Bhattacharya, S., Sehgal, N., et al. 2014, ApJ, 786, 13
- Vogelsberger, M., Genel, S., Springel, V., et al. 2014a, MNRAS, 444, 1518
- Vogelsberger, M., Genel, S., Springel, V., et al. 2014b, Nature, 509, 177
- Wang, J. & White, S. D. M. 2007, MNRAS, 380, 93
- White, M., Blanton, M., Bolton, A., et al. 2011, ApJ, 728, 126
- Zaldarriaga, M. & Seljak, U. 1997, Phys. Rev. D, 55, 1830
- Zaldarriaga, M. & Seljak, U. 1998, Phys. Rev. D, 58, 023003
- Zheng, Z., Zehavi, I., Eisenstein, D.J., et al. 2009, ApJ, 707, 554

matter power spectra, halo mass functions and linear halo biases.

Figure 19 plots the average matter power spectra measured from the six realizations for the 14 simulation-box

APPENDIX

A. MEASUREMENTS OF MATTER POWER SPECTRA, HALO MASS FUNCTIONS, AND HALO BIASES

In this appendix, we present comparisons of our simulation results to the theoretical fitting formulae for the

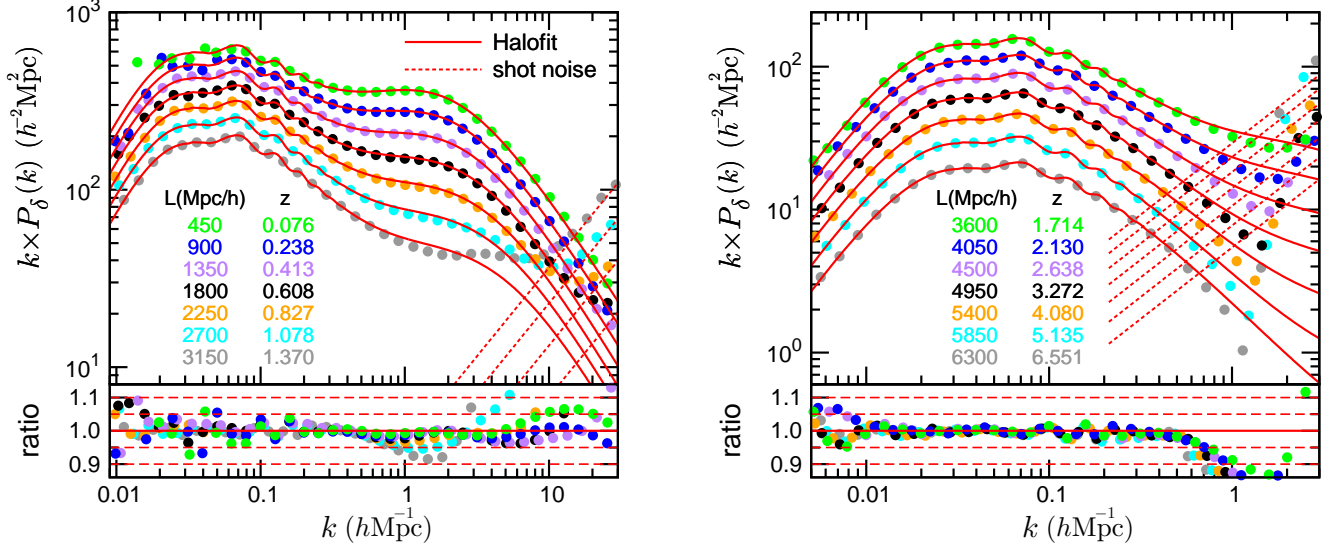


FIG. 19.— Matter power spectra $k \times P_\delta(k)$ as a function of wavenumber k for lower redshifts (left panel) and higher redshifts (right panel). The filled circles are the average simulation results of the six realizations with a bin width of $\Delta \log[k/(h\text{Mpc}^{-1})] = 0.1$. Each colored symbol corresponds to a separate redshift. The solid red curves are the revised Halofit, and the dotted red lines are the shot noise. The lower small panels plot ratios to the solid red curves. The dashed red lines denote 5% and 10% errors.

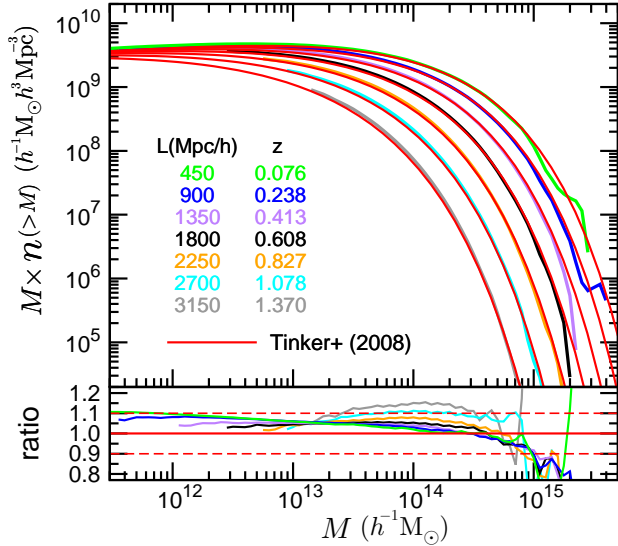


FIG. 20.— Halo mass functions $M \times n(>M)$ as a function of halo mass M for several redshifts, where $n(>M)$ is the cumulative halo number density. Each colored curve corresponds to the average simulation result of six realizations at each redshift. The red curves are the fitting formula of Tinker et al. (2008). The bottom panel plots ratios to the solid red curves.

sizes (see Section 2.1). Each redshift corresponds to the central dumped redshift of each box size (see Table 1). Here we do not subtract the shot noise from the measured power spectrum. The solid red curves are the theoretical fitting formula of the revised Halofit. The bottom panels show ratios to the red curves. The scatters seen at smaller k ($< 0.01 - 0.1 h\text{Mpc}^{-1}$) are caused by the sample variance. For relatively large k $\gtrsim 1 h\text{Mpc}^{-1}$, the simulation results decrease as a result of the lack of spatial resolution, which is more apparent for larger box-sizes. For very large k ($> 1 - 10 h\text{Mpc}^{-1}$), the simulation results increase as a result of the shot noise and approach the dotted lines. In the right panel, the dotted lines seem to fit the data poorly at intermediate scale $k \sim 1 h\text{Mpc}^{-1}$ be-

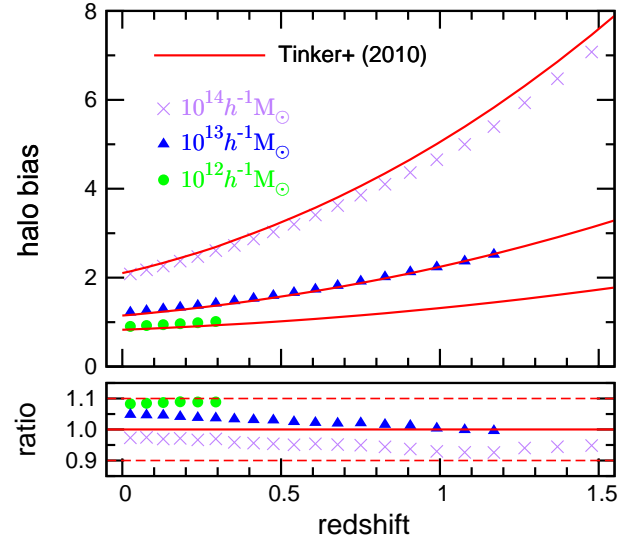


FIG. 21.— Linear halo biases as a function of redshift for $M = 10^{14} h^{-1} M_\odot$ (purple crosses), $10^{13} h^{-1} M_\odot$ (blue triangles), and $10^{12} h^{-1} M_\odot$ (green circles). These colored symbols are the average simulation results of six realizations, while the red curves are the fitting formula of Tinker et al. (2010). The bottom panel shows ratios to the solid red curves.

cause the simple shot-noise model (i.e., the inverse of the particle number density) overestimates the power, especially at higher redshifts (see e.g., Heitmann et al. 2010, Sections 4 and 6.2). The simulation results agree with the Halofit model within 5% – 10% up to $k = 3 h\text{Mpc}^{-1}$ and $0.6 h\text{Mpc}^{-1}$ for lower ($z \lesssim 1.5$) and higher redshifts ($z \gtrsim 1.5$), respectively.

Figure 20 shows the halo mass functions measured from the six N -body realizations for several redshifts. In the vertical axis, $n(>M)$ is the cumulative number density of halos heavier than M . Here we adopt M_{200b} as the halo mass M . Each colored curve is the average simulation result for each redshift, which is plotted for a halo mass higher than the minimum mass ($= 50 \times$ particle mass) in Table 1. The solid red curves are the theoretical fitting

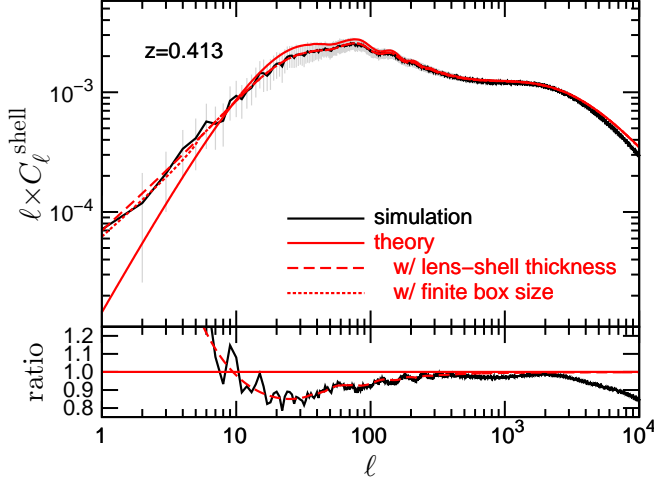


FIG. 22.— Angular power spectrum of the surface density on the lens shell at $z = 0.413$. The black curve gives the average of 108 simulation maps at $N_{\text{side}} = 8192$. The gray bars are the standard deviations. The dashed red curve shows the theoretical prediction including the finite thickness of the shell, while the solid red curve shows it without the correction. The dotted curve is the same as the dashed curve, but includes the effect of the finite-box size. The bottom panel shows ratios to the solid red curve.

formula of Tinker et al. (2008). For much higher masses ($M \gtrsim 10^{15} h^{-1} M_{\odot}$), the sample variance causes large scatter. The figure shows that the measured mass functions agree with the theoretical prediction within 10% up to $z = 1$.

Finally, Figure 21 plots the halo biases as a function of redshift for several halo masses. Here, the masses are binned with a bin size of 0.2 dex (i.e., $11.9 < \log[M/(h^{-1} M_{\odot})] < 12.1$ for $10^{12} h^{-1} M_{\odot}$). The linear halo bias is measured as the ratio of the halo power spectrum to the matter power spectrum, $b_{\text{h}}^2(M, z) = P_{\text{h}}(k; M, z)/P_{\delta}(k; z)$, in the linear regime where the wavenumber is set to be smaller than 10 times the fundamental mode (i.e., $k < 10 \times 2\pi/L$). We subtracted the shot noise from the measured halo power spectrum. There are no data points at higher redshifts for $M = 10^{12}$ or $10^{13} h^{-1} M_{\odot}$ because M is below the minimum halo mass at such high redshifts. The figure shows that the halo biases agree with the fitting formula of Tinker et al. (2010) within 10%.

B. MATTER POWER SPECTRUM CONVOLVED WITH THE WINDOW FUNCTION OF A SPHERICAL LENS SHELL

In this appendix, we discuss the effect of the lens-shell thickness on the angular power spectrum of density fluctuations. We consider a spherical shell with thickness Δr from a cubic simulation box, as shown in Figure 1. In the box, the mean density is $\bar{\rho}$ and the density contrast is $\delta(\mathbf{x})$. For a shell with an inner radius $r - \Delta r/2$ and an outer radius $r + \Delta r/2$, the surface density (in units of mass per steradian) is

$$\begin{aligned} \Sigma(\boldsymbol{\theta}) &= \bar{\rho} \int_{r-\Delta r/2}^{r+\Delta r/2} dr' r'^2 [1 + \delta(r'\boldsymbol{\theta}, r')], \\ &= \bar{\Sigma} [1 + \delta^{\text{shell}}(\boldsymbol{\theta})], \end{aligned} \quad (\text{B1})$$

where $\bar{\Sigma} = \bar{\rho} r^2 \Delta r$ is the mean surface density and

$$\delta^{\text{shell}}(\boldsymbol{\theta}) = \frac{1}{r^2 \Delta r} \int_{r-\Delta r/2}^{r+\Delta r/2} dr' r'^2 \delta(r'\boldsymbol{\theta}, r'), \quad (\text{B2})$$

is the density contrast on the shell. Here, the density contrast δ is given as a function of the radial coordinate r' and the tangential coordinate $r'\boldsymbol{\theta}$, and we assume that the thickness Δr is much smaller than the distance to the lens shell r . We derive the angular power spectrum of $\delta^{\text{shell}}(\boldsymbol{\theta})$ below.

The angular two-point correlation function of the density contrast on the shell is

$$\begin{aligned} \xi^{\text{shell}}(|\boldsymbol{\theta}_1 - \boldsymbol{\theta}_2|) &\equiv \langle \delta^{\text{shell}}(\boldsymbol{\theta}_1) \delta^{\text{shell}}(\boldsymbol{\theta}_2) \rangle \\ &= \frac{1}{(r^2 \Delta r)^2} \iint_{r-\Delta r/2}^{r+\Delta r/2} dr_1 dr_2 r_1^2 r_2^2 \int \frac{d^3 k}{(2\pi)^3} P_{\delta}(k) \\ &\times e^{-i(r_1 \boldsymbol{\theta}_1 - r_2 \boldsymbol{\theta}_2) \cdot \mathbf{k}_{\perp}} e^{-i(r_1 - r_2) k_{\parallel}}, \end{aligned} \quad (\text{B3})$$

where k_{\parallel} and \mathbf{k}_{\perp} are the parallel and perpendicular components of the wave vectors, respectively, and $P_{\delta}(k)$ is the matter power spectrum of the density fluctuation $\delta(\mathbf{x})$ as a function of $k = (k_{\parallel}^2 + |\mathbf{k}_{\perp}|^2)^{1/2}$. In the first exponential, we can approximately set $(r_1 \boldsymbol{\theta}_1 - r_2 \boldsymbol{\theta}_2) \cdot \mathbf{k}_{\perp} \simeq r(\boldsymbol{\theta}_1 - \boldsymbol{\theta}_2) \cdot \mathbf{k}_{\perp}$ with $r_1 \simeq r_2 \simeq r$. Then, Equation (B3) reduces to

$$\xi^{\text{shell}}(\theta) \simeq \int \frac{d^3 k}{(2\pi)^3} P_{\delta}(k) e^{-ir\boldsymbol{\theta} \cdot \mathbf{k}_{\perp}} \text{sinc}^2\left(\frac{k_{\parallel} \Delta r}{2}\right), \quad (\text{B4})$$

where $\text{sinc}(x) = \sin(x)/x$.

Therefore, the Fourier component of the correlation is

$$\begin{aligned} C_{\ell}^{\text{shell}} &= \int d^2 \theta \xi^{\text{shell}}(\boldsymbol{\theta}) e^{i\boldsymbol{\theta} \cdot \boldsymbol{\ell}} \\ &= \frac{1}{r^2} \int \frac{dk_{\parallel}}{2\pi} P_{\delta}(k) \text{sinc}^2\left(\frac{k_{\parallel} \Delta r}{2}\right), \end{aligned} \quad (\text{B5})$$

where $k = (k_{\parallel}^2 + |\mathbf{k}_{\perp}|^2)^{1/2}$ with $|\mathbf{k}_{\perp}| = \ell/r$. In the limit of infinite thickness, $k_{\parallel} \Delta r \rightarrow \infty$, Equation (B5) reduces to

$$\lim_{k_{\parallel} \Delta r \rightarrow \infty} C_{\ell}^{\text{shell}} = \frac{1}{r^2 \Delta r} P_{\delta}\left(k = \frac{\ell}{r}\right). \quad (\text{B6})$$

Therefore, the shell thickness influences surface density fluctuations comparable to or larger than Δr , but is negligible for fluctuations much smaller than Δr .

Figure 22 plots the angular power spectrum of the surface density on the shell at $z = 0.413$ with $\Delta r = 150 h^{-1} \text{Mpc}$. Here, $z \simeq 0.4$ is a typical lens redshift for the HSC survey ($z_s \simeq 1$). The solid black curve plots the average simulation result²⁴ calculated from the 108 maps at $N_{\text{side}} = 8192$. The dashed (solid) red curve represents the theoretical model with (without) the correction in

²⁴ Here, the simulation code GRAYTRIX adopted the cone-volume weighted distance $(3/4)[(r_2^4 - r_1^4)/(r_2^3 - r_1^3)]$ as the distance to the shell, which is slightly farther than the central distance of the shell r . This is because the volume (or the number of particles) in a farther shell with a half-radius from r to $r + \Delta r/2$ is slightly larger than a closer shell from $r - \Delta r/2$ to r . GRAYTRIX corrected this volume difference by introducing the new distance. See also Appendix C1 of Shirasaki et al. (2015).

Equations (B5) and (B6). Here, we employ the revised Halofit for the nonlinear matter power spectrum. The theoretical model in Equation (B5) agrees with the simulation results very well even for very low ℓ (see also the bottom panel). The shell thickness enhances the power at smaller scales ($\ell \lesssim 10$), but suppresses it at intermediate scales ($\ell \simeq 10 - 100$). This suppression appears to be less significant in the convergence power spectrum in Figure 5 and in the deflection-angle power spectrum in Figure 10; this occurs because three lens shells are used as a single set in the ray-tracing simulation, resulting in an effective shell thickness of $450 h^{-1} \text{Mpc}$, which somewhat mitigates the thickness effect. We confirmed that the theoretical model of Equation (B5) agrees with the simulation results at other redshifts from $z = 0.1$ to 7. However, for very low redshifts ($z < 0.1$), the simulation results show more suppression than the theoretical model of Equation (B5) at intermediate scale ($\ell \approx 10$) because our assumption of $\Delta r \ll r$ does not hold for nearby lens planes, and therefore Equation (B5) is less accurate.

We next comment on the effect of density fluctuations larger than the simulation-box-size L on the angular power spectrum on the lens shell (see also Sato et al. 2011; Harnois-Déraps & van Waerbeke 2015). In fact, the box does not include the fluctuations larger than L . In Figure 22, the dotted red curve is the same as the dashed curve, but with $P_\delta(k) = 0$ imposed at $k < 2\pi/L$ (here $L = 1350 h^{-1} \text{Mpc}$) in Equation (B5). As seen in the figure, the finite-box effect is not significant compared to the lens-shell thickness effect in our setting. The dashed and dotted curves agree completely at $\ell > 6$ and within 12% at $\ell \leq 6$. The difference is much smaller than the standard deviation (the gray bars) at large scales. The finite-box-size effect is more (less) significant at lower (higher) redshift because the box size is smaller (larger). The finite-box-size effect is smaller than the shell-thickness effect for $L = 900 h^{-1} \text{Mpc}$, but larger only for the second and third lens shells constructed from the $L = 450 \text{Mpc}$ box at $\ell < 5$. Therefore, we do not take the finite-box size into account throughout this paper²⁵.

In summary, we can take the shell thickness into account by replacing the matter power spectrum as follows:

$$P_\delta(k) \rightarrow P_\delta^W(k) = \Delta r \int \frac{dk_\parallel}{2\pi} P_\delta(k) \text{sinc}^2\left(\frac{k_\parallel \Delta r}{2}\right), \quad (\text{B7})$$

from Equations (B5) and (B6). As the integration in Equation (B7) is time consuming, we construct a simple fitting function for $\Delta r = 450 h^{-1} \text{Mpc}$ as

$$P_\delta^W(k) = \frac{(1 + c_1 k^{-\alpha_1})^{\alpha_1}}{(1 + c_2 k^{-\alpha_2})^{\alpha_3}} P(k), \quad (\text{B8})$$

with $c_1 = 9.5171 \times 10^{-4}$, $c_2 = 5.1543 \times 10^{-3}$, $\alpha_1 = 1.3063$, $\alpha_2 = 1.1475$, and $\alpha_3 = 0.62793$. The wavenumber k is in units of $h \text{Mpc}^{-1}$. The fitting formula agrees with the correct result within 0.7% at $z < 7.1$. Throughout this paper, we use the fitting function Equation (B8) to include the shell-thickness effect.

²⁵ One reason that the finite-box-size effect was significant in previous work (Sato et al. 2011) was that they adopted a smaller box size of $L = 240 h^{-1} \text{Mpc}$.

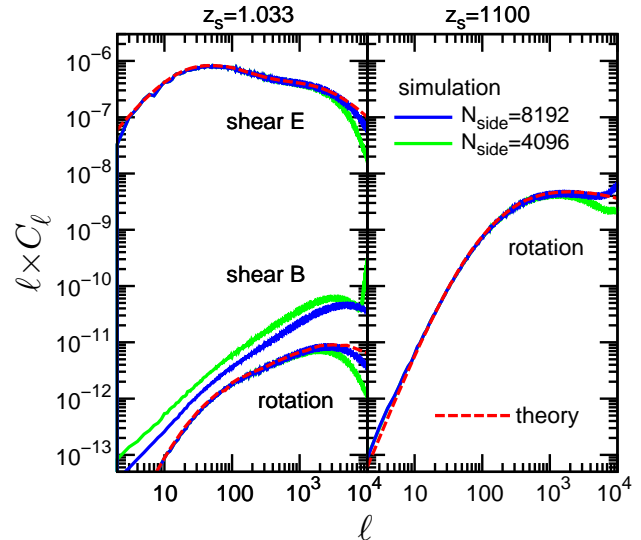


FIG. 23.— **Left panel:** angular power spectra of the shear E-mode (upper), B-mode (middle), and rotation (lower) at $z_s = 1.033$. Each curve gives the average of the 108 maps. The dashed red curves plot the theoretical predictions. **Right panel:** same as the left panel, but only for the rotation at $z_s = 1100$.

C. SMALL ANOMALIES IN OUR SIMULATION

In this appendix, we discuss the small anomalies appearing in the simulation maps, which can likely be attributed to a numerical error in our simulation.

The first anomaly is that the convergence at low redshift can be smaller than the minimum value predicted for the empty beam, which is simply obtained by setting $\delta = -1$ in Equation (3). The pixels with anomalous convergence are isotropically distributed over the sphere. This anomaly appears more frequently for lower source redshifts: the fraction of anomalous-convergence pixels in the all-sky maps is 0.33(0.22) at $z_s = 0.051$, 1.2×10^{-2} (3.9×10^{-4}) at $z_s = 0.10$, and 1.8×10^{-5} (5.2×10^{-8}) at $z_s = 0.16$ for $N_{\text{side}} = 8192$ (4096). Therefore, at $z_s > 0.1$, the fraction is negligibly small. In fact, there is no anomalous convergence at $z_s > 0.3$ in the 108 maps. This anomaly is probably caused by a numerical error in our simulation.

The second anomaly is an additional power seen in the shear B-mode power spectrum. The left panel of Figure 23 shows the angular power spectra of the shear E-mode (upper), B-mode (middle), and rotation (lower) at $z_s = 1.033$. The blue (green) curves show the averages of the 108 maps at $N_{\text{side}} = 8192$ (4096). The dashed red curves plot the theoretical predictions for the shear E/B-mode and rotation (Krause & Hirata 2010). The rotation power spectrum agrees closely with the theoretical prediction that the shear B-mode and rotation power spectra should be equal. However, the B-mode power spectrum has an additional power, which is probably caused by leakage from the E-mode to the B-mode. The discrepancy seems more prominent for lower angular resolution ($N_{\text{side}} = 4096$), suggesting that the anomaly is probably caused by numerical errors related to the angular resolution in the simulation. We note that the B-mode power is at least three orders of magnitude smaller than the E-mode power at $\ell = 2 - 10^4$; therefore, the additional B-mode power will be negligible for most practical purposes.

The right panel of Figure 23 is the same as the left panel, but for the rotation at $z_s = 1100$. Similar to the left panel, the rotation power spectrum agrees very well with the theoretical prediction.

D. GUIDE TO USING THE MOCK CATALOGS

Our mock catalogs can be used by visiting our website²⁶. It contains 108 realizations each for $N_{\text{side}} = 4096$ and 8192 and a single realization for $N_{\text{side}} = 16384$, which are labeled r000 to r107. These maps with the same label (r000 \sim r107) but different resolutions N_{side} derive from the same N -body data; correspondingly, they represent the same mass distribution, but simply differ in terms of angular resolution. The lower N_{side} mocks are less accurate but easier to handle. Three types of catalogs, as shown below, have been developed.

Weak lensing maps. These contain the convergence, shear, and rotation data on the full-sky sample from source redshift $z_s = 0.05$ to 5.3 (file ID number from zs1 to zs38) and at $z_s = 1100$ (zs66; see also Table.2). The data are given in the HEALPix pixelization with the

‘RING’ ordering (there are $12 \times N_{\text{side}}^2$ pixels on the full sky). Each map is $3.1 \text{ GB} \times (N_{\text{side}}/4096)^2$, as given in binary format. We include two codes (written in C and Fortran) for reading the binary file on the site. We also include a Fortran code to convert the binary file into the FITS format.

CMB maps. These contain the CMB temperature and polarization (Q and U) data. The data are given in the FITS format. We provide the 108 lensed CMB maps each for $N_{\text{side}} = 4096$ and 8192, and also provide the 108 unlensed CMB maps for $N_{\text{side}} = 8192$. We provide the data both for $\beta = 0$ and ω in Equation (2). The size of each map is $2.3 \text{ GB} \times (N_{\text{side}}/4096)^2$.

Halo catalogs. These contain the halo ID number, parent halo ID number, masses (M_{vir} , M_{200b} , M_{200c} , M_{500c} , and M_{2500c}), virial radius, scale radius, redshift, comoving distance, radial peculiar velocity, angular position on the sky in both image and lens plane, and the corresponding pixel number. The data are given in ASCII text format. Each catalog is 40 GB (independent of N_{side}). We also include the original ROCKSTAR halo catalogs on the site.

²⁶ http://cosmo.phys.hirosaki-u.ac.jp/takahasi/allsky_raytracing/